Chemical Engineering Journal Advances 5 (2021) 100060

Contents lists available at ScienceDirect

Chemical Engineering Journal Advances

journal homepage: www.elsevier.com/locate/ceja

Pseudo-image-feature-based identification benchmark for multi-phase flow regimes

Boyu Kuang [a,*], Somtochukwu Godfrey Nnabuife [b], Zeeshan Rana [a]

[a] Centre for Computational Engineering Sciences, Cranfield University, Cranfield, MK43 0AL, United Kingdom
[b] Geo-Energy Engineering Centre, Cranfield University, Cranfield, MK43 0AL, United Kingdom

ARTICLE INFO

Keywords:
Multiphase flow
Flow regime identification
Pseudo-image-feature
Deep learning classifier benchmark

ABSTRACT

Multiphase flow is a prevalent topic in many disciplines, and flow regime identification is an essential foundation in multiphase flow research. Computer vision and deep learning have achieved numerous excellent models, but many have not demonstrated satisfactory performance in fundamental research, including flow regime identification. This research proposes an advanced pseudo-image feature (PIF) as the flow regime descriptor and a benchmark of multiple deep learning classifiers. The PIF simulates the image format and compactly encodes the flow regime to a pseudo-image, which explicitly displays the implicit flow regime signals. This research further evaluates three proposed and five existing popular deep learning classifiers. The proposed benchmark provides a baseline for applying deep learning in flow regime identification. The proposed fully convolutional network (FCN) classifier achieved state-of-the-art performance, and the testing and verification accuracy respectively reached 99.95% and 99.54%. This research suggests that PIF has an excellent capability for flow regime representation, and the proposed deep learning classifiers achieve superior performance in flow regime identification compared to the existing classifiers. Industries can utilize the proposed multiphase flow identification technology to obtain greater production efficiency, productivity, and financial gain.

1. Introduction

Fluid flows concurrently inside the pipelines in a wide range of industrial and engineering processes. Gas-liquid flows exist in chemical and petrochemical plants, condensers, power generation, nuclear energy facilities, steam boilers, food processing, thermal engineering, and chemical reactors [1,2]. For accurate design and the operation of two-phase gas-liquid flow facilities, accurate prediction of the system's pressure and pressure drop is required, and that prediction relies on a proper understanding and knowledge of the nature of the flow regimes in the system. In the production system, it is necessary to identify unwanted flow regimes in the conduit in a timely manner to help the flow control system handle them on time and prohibit unwanted flow regime formation, such as a slug flow in the pipeline system. If a harmful flow regime, like a slug flow, is not detected on time, it can harm the platform equipment or even cause the plant to shut down [3].

Flow regime recognition has been extensively studied in recent years. One of the identification techniques is the application of invasive point sensors such as electrical or fiber optic, the hot wire anemometer, and pitot tubes [4–7]. The drawback of these techniques is the flow field, which is usually locally disturbed; furthermore, the boundaries between different flow regimes are subjectively defined [8].

The deployment of multiple sensors is another technique for the identification of flow regimes. Multiple sensors enhance the phase distribution's temporal and spatial resolution and help to identify the flow regime's features [9,10]. Multiple sensor applications require signal fusion, which improves the predictability of flow regimes. Multiple sensors' typical arrangement with appropriate signal processing and phase-field reconstruction is often referred to as tomographic measurement [11–13]. Although tomographic principles have been studied for years, it is not yet widely accepted because it is capital intensive and has limited applications.

The tomography-based method is attractive because it is a non-invasive and non-intrusive signal acquisition from sensors situated on the edge of the vessel or pipeline. It provides the spatial distribution of the interfaces between different phases [14]. Tomographic methods based on radiation sources such as γ-ray and x-ray have high imaging and spatial resolution accuracy, have received much attention, and have been applied in chemical, nuclear engineering, and food industries [15]. Kumar et al. [16] review γ-ray and x-ray tomography applications in two-phase flow systems, demonstrating that it is costly and that its slow response hinders its broad application in industries. The applicability of tomographic methods must be restricted to ensure the safety of the

* Corresponding author.
E-mail addresses: neil.kuang@cranfield.ac.uk (B. Kuang), g.nnabuife@cranfield.ac.uk (S.G. Nnabuife), zeeshan.rana@cranfield.ac.uk (Z. Rana).

https://doi.org/10.1016/j.ceja.2020.100060
Received 28 October 2020; Received in revised form 21 November 2020; Accepted 21 November 2020

operators. Alternatively, harmless methods for routine use include capacitance [17–19], optical [20,21], and ultrasound techniques [22,23].

Considering that multiphase flow regimes' apparent features are usually hidden within random signal variations acquired through the deployment of a measuring instrument, signal analysis is highly paramount in the identification of various flow regimes. The extracted features from random flow signals are employed for the identification of flow regimes using some rule-based systems [24]. Although much research has been conducted to make the classification of flow regime perception bias-free, total objective flow regime identification has yet to be achieved. Moreover, to reduce the subjectivity of flow regime identification, various signal processing methods have been used [25,26] such as machine learning [27,28], soft computing methods [29–32], and statistical methods [33].

Classification is an interesting topic in computer vision and deep learning. Simonyan & Zisserman [34] discuss the influence of the increasing depth in the convolutional neural network (CNN) on pattern recognition and proposes the VGG (Visual Geometry Group) model to adapt to this increased depth. However, He et al. [35] observe that the increased depth introduces network degradation, so they propose the residual neural network (ResNet) to handle it. The DenseNet dramatically reduces the CNN scale, enhances the utilization of the feature map, and reduces the vanishing gradient [36]. The MobileNet focuses on the feasibility of neural networks on mobile and embedded devices [37]. Moreover, Zoph and Shlens [38] further propose the NASNet, which attempts to utilize one neural network to design another.

Although much research has been conducted on two-phase flow regime recognition in different single pipeline configurations such as horizontal pipes, inclined pipes, or vertical pipes, a limited amount of research has been carried out on complex pipeline configurations such as S-shaped, U-shaped, Lazy S-shaped, and catenary [3]. In this paper, an ultrasonic sensor and deep learning method are applied to classify different flow regimes in a two-phase gas-liquid S-shaped pipeline-riser system.

Deep learning has demonstrated remarkable capability in signal processing and pattern recognition, which has led to numerous achievements in image classification, autonomous driving, and human behavior analysis [39,40]. Most of the current popular classifiers are trained using the ImageNet [41], such as VGG, ResNet, DenseNet, MobileNet [37], and NASNet [38]. For further reading, other related works can be found in [42–46]. This paper proposes the applicability of transferring computer vision and deep learning technologies into the popular and challenging multiphase flow regime identification.

This paper aims to identify the gas-liquid two-phase flow regime in an S-shape pipe, which is a typical case in the multiphase flow industries. When liquid and gas flow through a pipe, different flow patterns can be observed, such as annular, bubbly, churn, or slug flows [24]. The conventional flow regime identification method uses the vision recognition method [47,48], mostly affected by experience and human factors. Thus, the efficiency and reliability are highly limited [49].

The contributions of this paper are summarized as follows: First, it proposes a new feature extraction algorithm for the two-phase flow ultrasonic signal's preprocessing, the pseudo-image feature (PIF) extraction algorithm. Second, it proposes a flow regime identification benchmark using the PIF and various deep learning classifiers (three proposed and five existing popular classifiers). Third, this paper encodes the flow regime signals into the pseudo-image format, which displays the implicit signals with an explicit formation. This research further visualizes, in graphical form, the data flow in the proposed fully convolutional network (FCN) classifier to facilitate the analysis.

2. Measurement sensor and specification

The Doppler effect is the frequency fluctuation of an acoustic wave when there is movement between the source and the acoustic receiver, where the frequency change is proportional to the source acoustic velocity [50]. The source acoustic velocity is acquired by estimating the shift in frequency between the source and the acoustic receiver as illustrated in Fig. 1(b). In the Doppler flowmeter, an acoustic beam is continuously released from the transducer into the flow. The beam is then reflected by the moving fluid scatterers, which could be bubbles in the flow [51]. The scattered fluid acoustic beam is then received by another ultrasonic transducer, and the fluid velocity is calculated with the frequency shift based on Doppler effects.

The ultrasonic Doppler used in this paper is DFM-2, a commercial, non-intrusive flowmeter. It acquires the ultrasonic raw signals, calculates the shift in Doppler frequency of the ultrasonic signals reflected from fluid discontinuities like bubbles in the flowing fluid, and estimates the flow velocity [24,52]. Other specifications of the flow meter used in the experiment are given in Tab. 1.

3. Test rig and experimental procedure

3.1. Two-phase flow test rig setup

The experiment was carried out on a multiphase flow S-shaped riser at Cranfield University's oil and gas center. The 2 inch multiphase flow system contained a 40 m horizontal pipeline, 5.5 m vertical pipe lower section, 1.5 m downcomer, 3.5 m topside section, and 5.7 m vertical upper section [53]. The S-shaped multiphase loop test section had a transparent pipe for visual observation of the flow regime. The multiphase flow loop was controlled using DeltaV, a Fieldbus-based supervisory control and data acquisition (SCADA) software provided by Emerson Process Management. The schematic representation diagram of the multiphase flow loop is depicted in Fig. 2. The bank of two compressors connected in parallel supplied the air to the test loop. The air from the two compressors was collected in an 8 m^3 capacity receiver to minimize the pressure variation from the compressor. The air from the receiver passed through the coarse, fine, and medium filters, and then through a cooler, where condensates present in the air were removed [24]. A 12.5 m^3 capacity water tank supplied the water to the flow facility employing two multistage Grundfos CR90-5 pumps. The water pump had a duty of 100 m^3/hr at 10 bar and was metered by a 1-inch Rosemount 8742 magnetic flow meter (up to 7.36 l/s) and a 3 inch Foxboro CFT50 Coriolis meter (up to 30 kg/s).

3.2. Ground-truth dataset

The ground-truth data used in this paper are from an open dataset, the two-phase flow Doppler signals dataset, which can be found on Cranfield Online Research Data (CORD). The specific details of the experiment are not the focus of this paper, and can be found in [53]. This section focuses on the format of the data.

The ground-truth data were acquired from 125 ground-truth experiments with different gas-liquid ratio settings. The data recording time for each experiment was about two minutes, and 1.3 million discrete Doppler signal digits were collected in each experiment. In this way, the original ground-truth data used in this study could be understood as 125 one-dimensional vectors, each vector with a length of 1.3 million digits. Notably, the maximum frequency of the gas-liquid flow Doppler signal should have been lower than 2 kHz according to the physical limitations of the ground-truth experiment rigs. Each experimental datum has been labeled the ground-truth flow regime using the objective method.

4. Data preprocessing

4.1. Pseudo-image feature (PIF) algorithm

The proposed PIF extraction algorithm describes the flow regime more explicitly. The ultrasonic Doppler signal obtained from Section 3 is

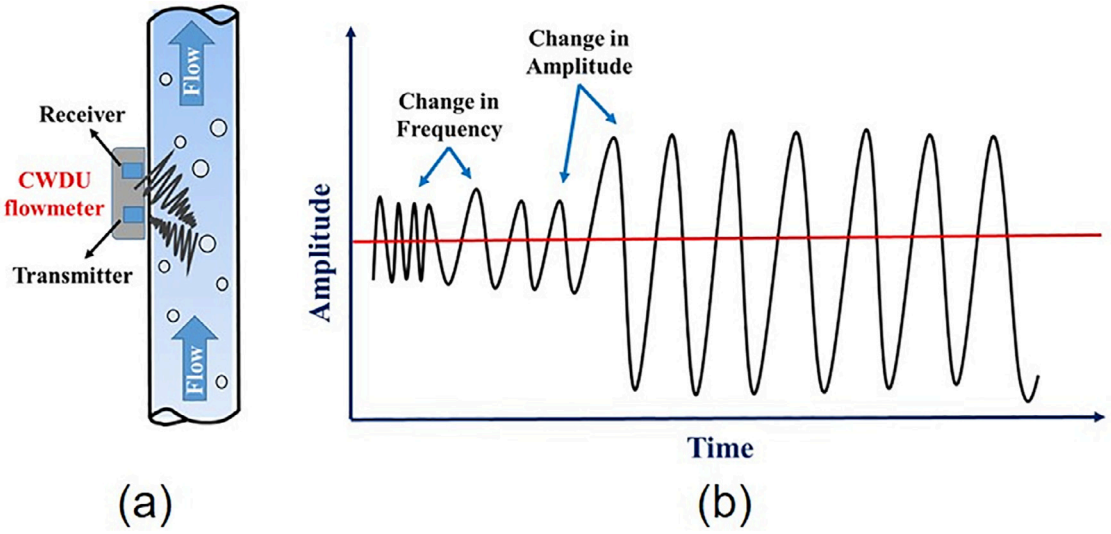

Fig. 1. Ultrasound Doppler principle. [24].

Tab. 1
Continuous-wave ultrasonic Doppler flowmeter specifications

Model	DFM-2
Maker	United Automation Ltd., Southport, U.K.
Analogue output	Active 4-20 mA
Velocity range	0 to 19.99 feet per second velocity by Liquid Crystal Display (LCD).
Repeatability	1% of reading.
Indicator	Sufficient signal strength only when the green Light Emitting Diode (LED) is on
Temperature	Instrument 0 to 50°C. Standard sensor -30 to 70°C. HT sensors are available up to 120°C.

a 1D time-domain signal. Fig. 3(a) (a) illustrates the raw data with waveform. It is clear that the original time-domain signal is a complex and unintuitive representation, and it is difficult to directly read the valid information. Moreover, the original signal only correlates along a single dimension (the time axis). The PIF extraction algorithm builds more information correlation in higher dimensions, which describes the flow regime information in a more compact but explicit way. A digital image is composed of multiple channels of image layers, the data in each layer containing the 2D correlations (height and width axis). The data between different image layers are independent of each other, and the different layers are named as the different channels. This research imitated the image structure and constructed the flow state signal into a pseudo-image structure, because the image is an intuitive signal.

According to Nyquist's theorem, a wavelength greater than twice the highest frequency contains all the information of a complete cycle. Therefore, another task of the preprocessing phase is to reasonably expand the number of samples used for the ensuing deep learning classifiers training. The PIF extraction algorithm also uses a twin-window strategy, which is similar to the twin-window feature extraction (TFE) algorithm [24]. Fig. 3 depicts the detailed process of the PIF extraction algorithm (the pseudocode of the PIF extraction algorithm can be found in the Appendix). Fig. 3(a) red region corresponds to the data formation. Fig. 3(b) uses a single experimental record as an example.

The first step is shown in Fig. 3(b) (the green box). The PIF algorithm uses window A to intercept a part of the original experimental data. The amount of data intercepted by window A is the information capacity available for a single PIF.

The second step is illustrated in Fig. 3(c) (the blue box) and Fig. 3(d) (the purple box). The PIF algorithm further uses window B to intercept a portion of the data from window A, then fast-Fourier transforms the Doppler signal from the time domain to the frequency domain. The PIF further uses another smaller window (window B) to prevent amplitude leakage from the FFT. Window B slides and traverses the entire window A. Subsequently, the frequency domain transform results of all window Bs are averaged and counted as the pseudo-image feature of one channel (as shown in Fig. 3[d]). Eq. (1) illustrates the numerical relationship between L_{WB} and the feature value in the corresponding channel. While $feature_C$ refers to the feature value in channel No. C, N_{WB} refers to the amount of window B. *fft* refers to the fast Fourier transform operation. L_{WBi} refers to the length of window B No. i, and N_{fft} refers to the sampling amount of FFT.

$$feature_c = \frac{\sum_1^{N_{WB}} fft(L_{WBi},\ N_{fft})}{N_{WB}} \tag{1}$$

Fig. 3(e) (the red box) illustrates the fourth step. Notably, PIF's aim is to summarize and reserve the distinguishment among the flow regime's signals instead of restoring the general information. This research transforms the tediously long 1D information association into a compact, higher-dimensional information association. In an individual PIF channel, the height axis distributes various frequency ranges from low to high, while the width axis distributes the frequency from low to high. Thus, each channel corresponds to a specific frequency distribution in a 2D format. The channel axis distributes the value of N_{fft}, which explicitly corresponds to the FFT sampling resolution. This 3D format compactly and explicitly encodes the flow regime information.

4.2. Pseudo-image-feature (PIF) experiments

Fig. 3(e) shows the eventual PIF, which is remarkably similar to the structure of the real image. This research used the strategy of the control variates to study the impact of the PIF hyper-parameters. Table 2 displays the experimental settings; this section focuses on the design theory for each hyper-parameter.

The step size of window B (S_{WB}) represents the overlapping length of the adjacent window Bs, which directly corresponds to the number of window Bs in a single window A (N_{WB}). Eq. (2) indicates the numerical

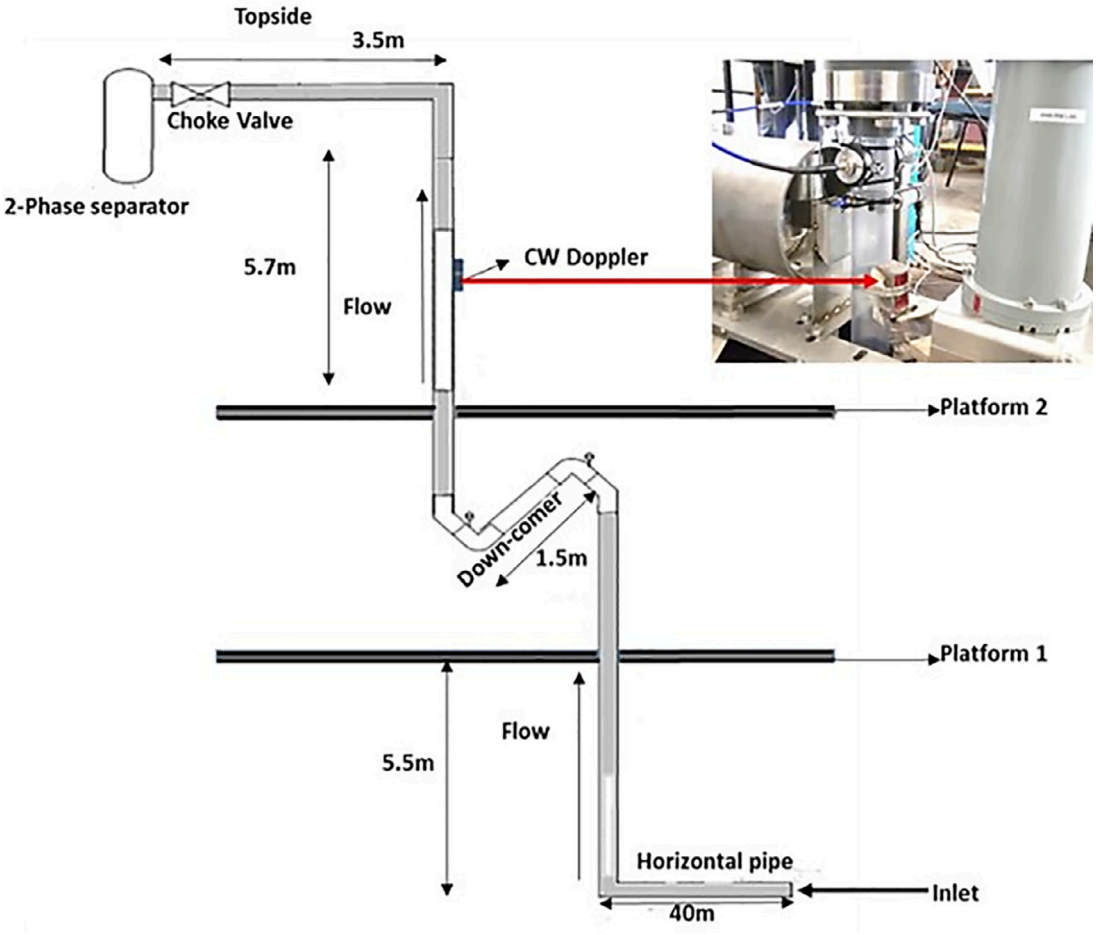

Fig. 2. Schematic diagram of the S-shape rig. [24].

Tab. 2
The PIF hyper-parameters experimental settings on the flow regimes dataset. While "idx" refers to the experimental index, "h", "w", and "c" respectively correspond to the height, width, and $\boldsymbol{N_{channel}}$ of the output PIF. The "/" represents not applicable. "5,120–8,192" refers to a range between 5,120 and 8,192 digits.

idx Unit	L_{WB} digits	N_{WB} WB	(h, w, c) digits	N_{fft} /	L_{WA} digits	S_{WA} digits	N_{PIF} PIFs
1	5,120-8,192	**8**	(1*256*9)	512	30,000	2,500	63,500
2	5,120-8,192	**8**	(1*256*9)	512	**50,000**	2,500	62,500
3	5,120-8,192	**16**	(1*256*9)	512	**30,000**	2,500	63,500
4	5,120-8,192	**24**	(1*256*9)	512	50,000	2,500	62,500
5	5,120-8,192	16	(1*256*17)	512	**30,000**	2,500	63,500
6	5,120-8,192	16	(1*256*17)	512	**50,000**	2,500	62,500
7	5,120-8,192	16	(1*1,024*7)	**2,048**	50,000	2,500	62,500
8	5,120-8,192	16	(1*512*7)	**1,024**	50,000	2,500	62,500
9	5,120-8,192	16	(1*512*7)	**1,024**	50,000	2,500	62,500
10	5,120-8,192	16	(1*256*7)	**512**	50,000	2,500	62,500
11	5,120-8,192	16	(1*1,024*3)	**2,048**	**50,000**	**2,500**	62,500
12	5,120-8,192	16	(1*512*3)	**1,024**	50,000	2,500	62,500
13	5,120-8,192	16	(1*256*3)	**512**	50,000	2,500	62,500
14	5,120-8,192	16	(1*128*3)	**256**	50,000	2,500	62,500
15	5,120-8,192	16	(1*1,024*3)	2,048	**30,000**	2,500	63,500
16	5,120-8,192	16	(1*1,024*3)	2,048	**10,000**	2,500	64,500
17	5,120-8,192	16	(1*1,024*3)	2,048	**100,000**	2,000	75,000
18	5,120-8,192	16	(1*256*9)	512	30,000	**1,250**	127,000
19	5,120-8,192	16	**(1*1,024*3)**	2,048	50,000	**1,250**	125,000
20	5,120-8,192	16	**(48*64*1)**	2,048	50,000	1,250	125,000
21	5,120-8,192	16	**(32*32*3)**	2,048	50,000	1,250	125,000

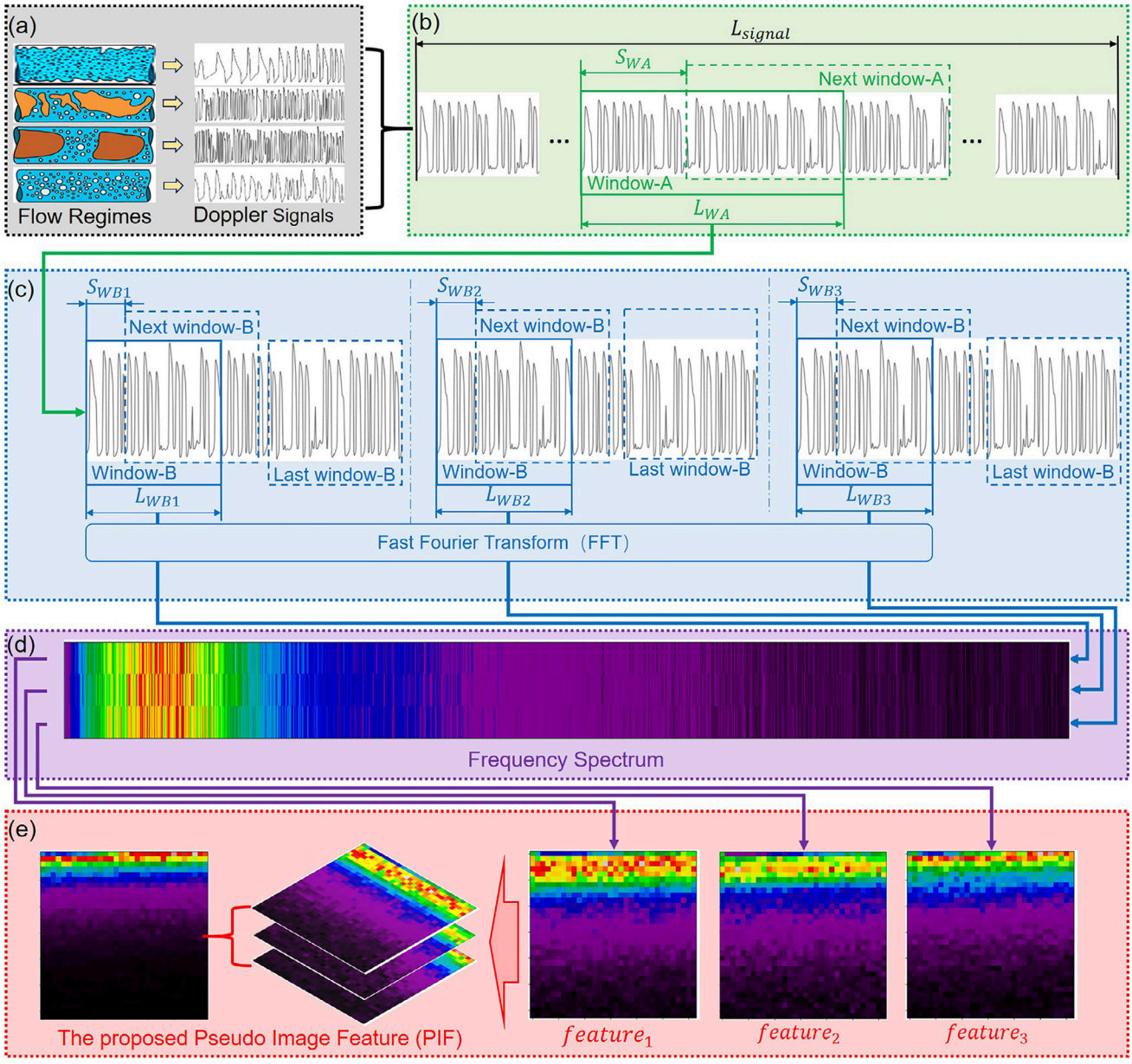

Fig. 3. Illustration of the process of the PIF algorithm for one pseudo-image feature. (a) refers to the flow regime dataset discussed in Section 3. (b), (c), (d), and (e) depict the preprocessing phase in Section 4. (b) refers to the window A process in the PIF algorithm; (c) refers to the window B process in the PIF algorithm. (d) shows the frequency spectrum from the fast Fourier transform. (e) simulates the image form and encodes the pseudo-image feature.

relationship between S_{WB} and N_{WB}. The two ends of the FFT had amplitude leakage, which this study used the twin-window strategy [24] to overcome. Although small S_{WB} can greatly reduce the amplitude leakage, the corresponding averaging smoothness S_{WB} decreases the details of the flow regime, which suppresses the ability to further improve accuracy. Experiments (1), (2), (3), and (4) tested four different N_{WB} values: 8, 16, 24, and 48 window Bs.

$$N_{WB} = \frac{L_{WA} - L_{WB}}{S_{WB}} + 1 \tag{2}$$

The length of window A (L_{WA}) corresponds to the maximum information available for encoding an individual PIF. Small L_{WA} decreases the representation capability of the PIF. Large L_{WA} increases the N_{WB}, which increases the averaging smoothness. That is the main reason the TFE algorithm [24] is difficult to further improve. This study compared the effects of L_{WA} through Experiments (2), (3), (5), (6), (11), (15), (16), and (17). The maximum L_{WA} was 50,000 digits, which was the value used in the TFE algorithm [24].

The length of window B (L_{WB}) corresponds to the length for one FFT. According to the Nyquist theorem, the signal length of the frequency domain transform should be as close as possible to twice the maximum frequency. It normally sets a value between 2.36 and 4 in practical use, which corresponds to the range of 5,120 to 8,192 digits in this research.

The change rate of the length of window B (Δ_{LWB}) corresponds to the number of channels ($N_{channel}$) for a single PIF. Eq. (3) indicates the numerical relationship between $N_{channel}$ and Δ_{LWB}, where L_{WB-max} and L_{WB-min} represent the maximum and minimum L_{WB}. Experiments (3), (5), (6), (7), (11), and (13) chose three different channel amounts: 3, 9, and 17 channels.

$$N_{channel} = \frac{L_{WB-max} - L_{WB-min}}{\Delta_{LWB}} + 1 \tag{3}$$

Table 3
The result of the experiments in Tab. 2. "idx" refers the experimental index. acc_{train}, acc_{test}, and acc_{valid} respectively refer to the training, testing, and validation accuracy. $loss_{train}$, $loss_{test}$, and $loss_{valid}$ respectively refer to the training, testing, and validation loss. "cce" refers to the categorical cross entropy, while "mse" refers to the mean squared error. "cb" refers to the call-back points for various experiments, the unit being epochs. "lr" refers to the learning rate. The bold values refer to the best results.

	acc_{train}	$loss_{train}$		acc_{test}	$loss_{test}$		acc_{valid}	$loss_{valid}$			
idx	(%)	cce	mse	(%)	cce	mse	(%)	cce	mse	cb(epoch)	lr
1	94.89	0.1291	0.0186	88.41	0.3255	0.0438	88.71	0.3140	0.0423	500	0.00001
2	96.88	0.0808	0.0116	91.90	0.2229	0.0305	92.39	0.2108	0.0286	500	0.00001
3	93.99	0.1474	0.0215	91.22	0.2233	0.0320	91.33	0.2193	0.0320	500	0.00001
4	97.47	0.0662	0.1438	94.93	0.1438	0.0194	94.30	0.1570	0.0212	500	0.00001
5	89.93	0.2439	0.0357	91.03	0.2164	0.0320	90.07	0.2439	0.0359	64	0.00001
6	95.18	0.1226	0.0179	92.78	0.1847	0.0270	91.89	0.1980	0.0291	592	0.000005
7	99.61	0.0123	0.0015	99.47	0.0157	0.0021	99.45	0.0172	0.0022	186	0.00001
8	99.7	0.0084	0.0011	97.52	0.0913	0.0103	97.27	0.1013	0.0112	147	0.00003
9	97.97	0.0548	0.0076	94.61	0.1594	0.0210	94.63	0.1721	0.0218	365	0.00001
10	94.31	0.1434	0.0209	81.51	0.2211	0.0315	91.10	0.2242	0.0322	147	0.00001
11	99.37	0.0187	0.0024	99.49	0.0171	0.0024	99.34	0.0197	0.0027	201	0.00001
12	99.46	0.0159	0.0021	97.96	0.0662	0.0087	97.60	0.0738	0.0093	197	0.00003
13	98.15	0.0486	0.0069	93.81	0.1949	0.0247	93.71	0.1859	0.0239	237	0.00001
14	91.18	0.2082	0.0308	90.50	0.2244	0.0344	91.22	0.2084	0.0309	40	0.00003
15	99.88	0.0044	4.9295 *e-4	99.22	0.0245	0.0030	99.35	0.0210	0.0027	149	0.00003
16	86.91	0.3236	0.0469	82.66	0.4818	0.0661	82.02	0.5043	0.0683	30	0.00003
17	99.93	0.0030	3.2469 *e-4	99.93	0.0015	2.1949 *e-4	99.94	0.0013	1.8122 *e-4	500	0.00001
18	95.28	0.1172	0.0171	93.29	0.1762	0.0249	93.11	0.1744	0.0251	1000	0.000008
19	**99.70**	0.0093	0.0012	**99.66**	0.0105	0.0013	**99.65**	0.0101	0.0013	500	0.00001
20	**99.69**	0.0093	0.0012	**99.66**	0.0105	0.0013	**99.65**	0.0101	0.0013	500	0.00001
21	**97.20**	**0.0180**	**0.0104**	**97.66**	**0.0599**	**0.0087**	**97.77**	**0.0553**	**0.0081**	**300**	**0.00001**

The step length of window A (S_{WA}) directly corresponds to the total amount of PIF (N_{PIF}) that can be generated. Eq. (4) represents the numerical relationship between the length of a single experimental datum (L_{signal}), L_{WA}, S_{WA}, and N_{PIF}. The original signal is particularly long and contains multiple cycles, and it is reasonable to divide it into smaller pieces. Large S_{WA} decreases the N_{PIF}, which causes more risks for overfitting in the ensuing deep learning training. Small S_{WA} creates too many similar PIF samples, which is not helpful for deep learning training. This study compared the effects of different S_{WA} on PIF performance through Experiments (11), (18), and (19). It used 125% and 62.5% of the maximum frequency for the S_{WA}, which ensured enough differentiation between adjoining PIFs.

$$N_{PIF} = \frac{L_{signal} - L_{WA}}{S_{WA}} + 1 \tag{4}$$

The experiments for all hyper-parameters of the PIF algorithms were tested using the DNN-based classifier proposed in Section 4.

5. Deep learning classifiers

Ten classifiers (from eight deep learning architectures) were tested with the PIF, which included the three proposed classifiers and five existing popular classifiers. Based on the test results of these 10 deep learning classifiers, this paper proposes a benchmark for the gas-liquid two-phase flow regime identification. This section focuses on the three proposed classifiers: the classifier based on the deep neural network (DNN), that based on the convolutional neural network (CNN), and that based on the fully convolutional network (FCN). They all demonstrated better performance in flow regime identification than the other seven existing classifiers.

To ensure the fairness and comparability of the experiments in Tab. 3, this paper only uses the DNN-based classifier to evaluate all the PIF hyper-parameter settings.

5.1. Proposed DNN-based classifier

Fig. 4 illustrates the structure of the proposed DNN-based flow regime classifier. The fully connected neural network has excellent data analysis capability, so it is a suitable evaluator for the experiments in Tab. 1. The DNN classifier has four hidden layers, and each hidden layer is followed by a LeakyReLU activation layer, a batch normalization layer, and a dropout layer with a rate of 20%. The four hidden layers respectively lay out with 2,048, 2,048, 1,024, and 1,024 neurons, which represents a gradually tightening structure. The green area is the output layer with the Softmax activation.

5.2. Proposed CNN-based classifier

Fig. 5 displays the structure of the CNN-based flow regime classifier. As introduced in Section 4.1, the PIF algorithm builds the information associations in the higher dimensions (height, width, and channel dimension); however, the DNN classifier does not make full use of the information associations. The proposed CNN-based classifier consists of a convolutional part and a fully connected part. The convolutional part builds the deep associations through the convolutional kernels, while the fully connected part collects the information from the convolutional part. Fig. 5(b) illustrates the convolutional part, which contains seven convolutional layers. The stride value in the even layers is two. The first six convolutional layers all consist of a zero-padding layer, a convolutional layer, and a LeakyReLU activation layer. The last convolution has only one convolutional layer and one LeakyReLU activation layer. The orange cube in Fig. 5(c) depicts a flattened layer: the output of the convolution part is flattened into a one-dimensional vector and inputted into the fully connected part. Because the convolution part conducts the information refining, the fully connected part can be on a smaller scale. Fig. 5(c) illustrates the fully connected part, which contains two hidden layers, each hidden layer containing 1,024 neurons.

5.3. Proposed FCN-based classifier

The left side of Fig. 6 illustrates the proposed FCN-based classifier. The FCN-based classifier only uses the convolutional structures. In addition, the parameter sharing of the convolution operation makes the FCN classifier more robust to the input size. The left side of Fig. 6 contains 11 hidden convolutional layers. The first six hidden layers follow the pattern of a zero-padding layer, a convolutional layer, and a LeakyReLU

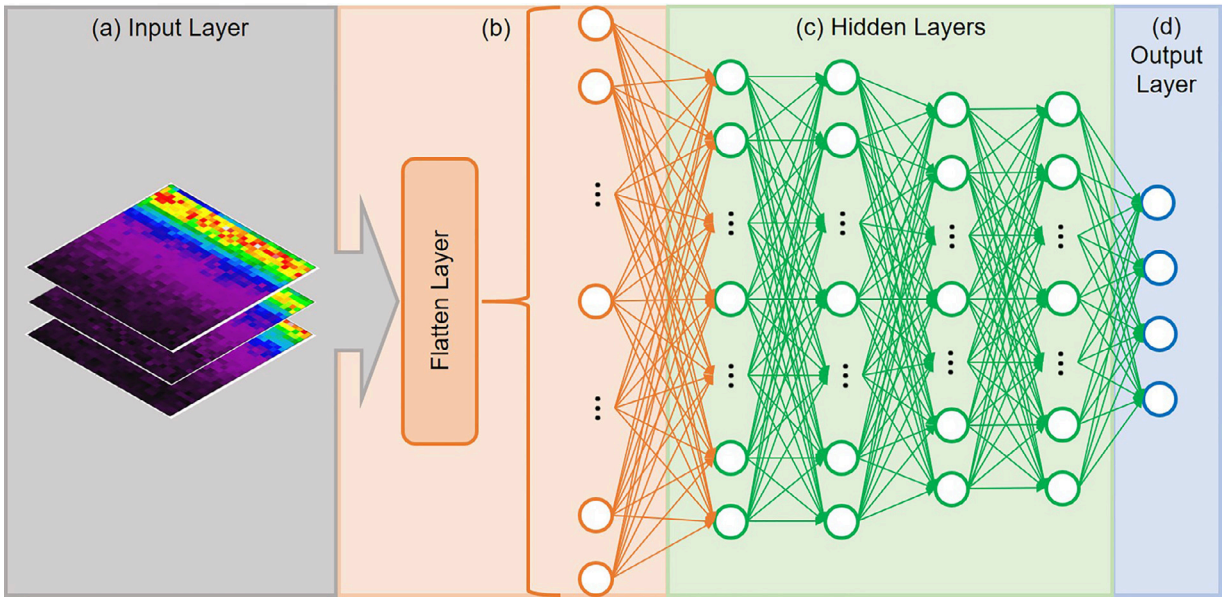

Fig. 4. The structure of the proposed DNN-based flow regime classifier. (a) (the grey region) contains the PIF with a size of 32 digits in height, 32 digits in width, and 3 channels. (b) (the orange region) refers to the input layer. (c) (the green region) refers to the hidden layers. (d) (the blue region) refers to the output layer.

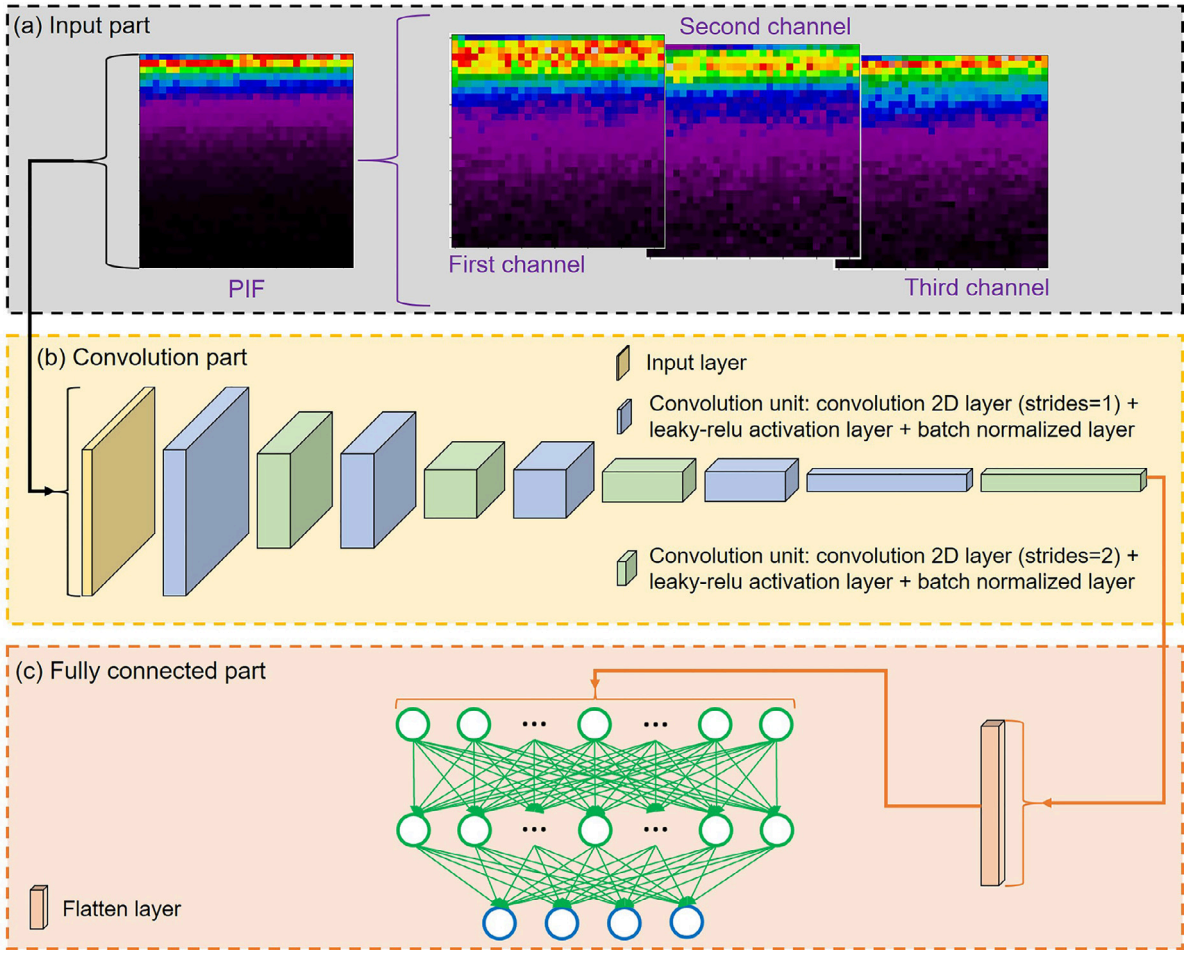

Fig. 5. The structure of the proposed CNN-based flow regime classifier. (a) (the grey region) refers to the PIF data from Section 4.2. (b) (the yellow part) refers to the convolution part. (c) (the orange part) refers to the fully connected part. The yellow cube refers to the input layer, the blue cubes refer to the odd convolution layers, the green cubes refer to the even convolution layers, the orange cube refers to the flatten operation, the green nodes refer to the two hidden layers, and the blue nodes refers to the output layer.

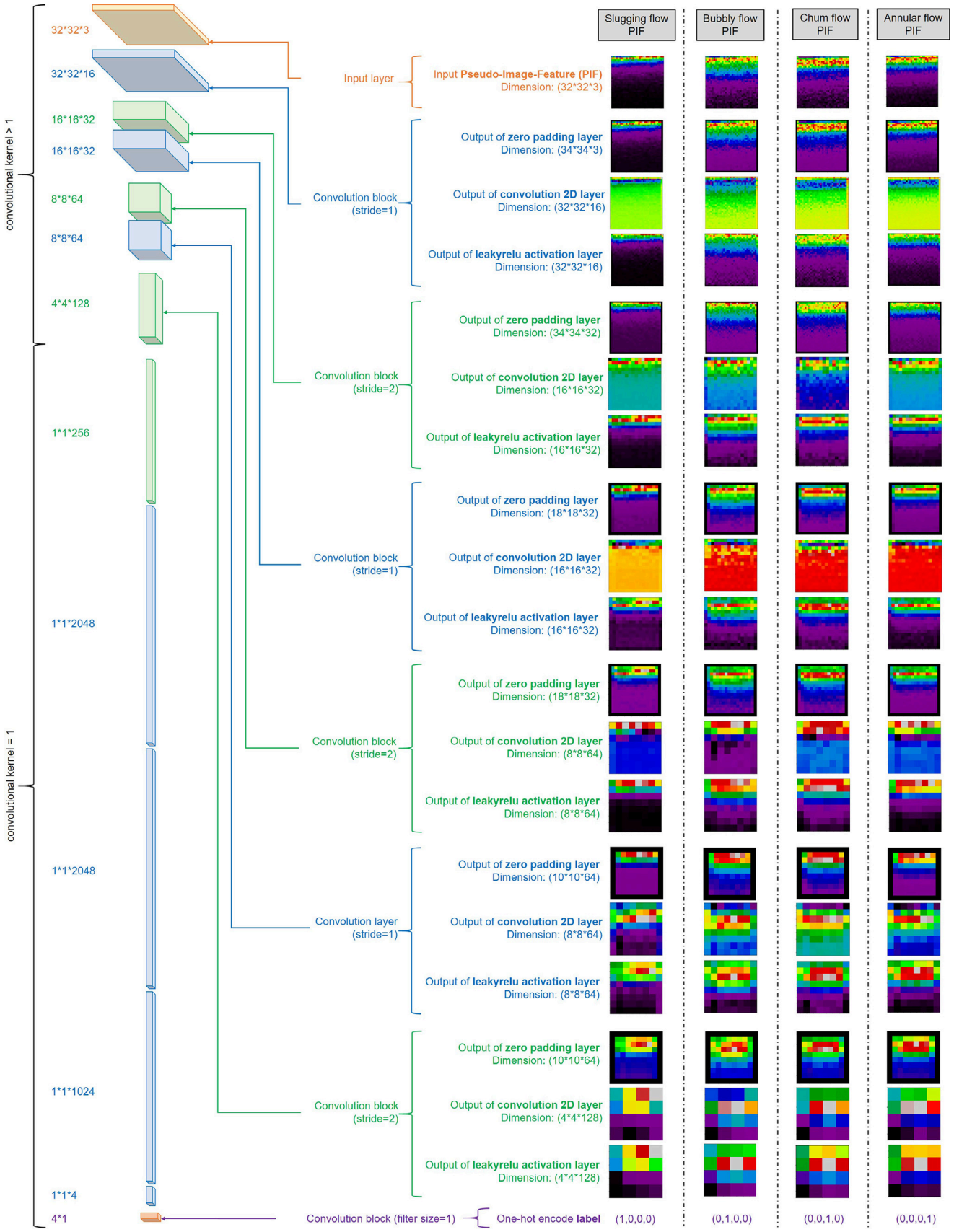

Fig. 6. The structure of the proposed FCN and the process visualization of the convolutional blocks. The unit of the tensor dimension is digits. The entire visualization has been resized for proper display.

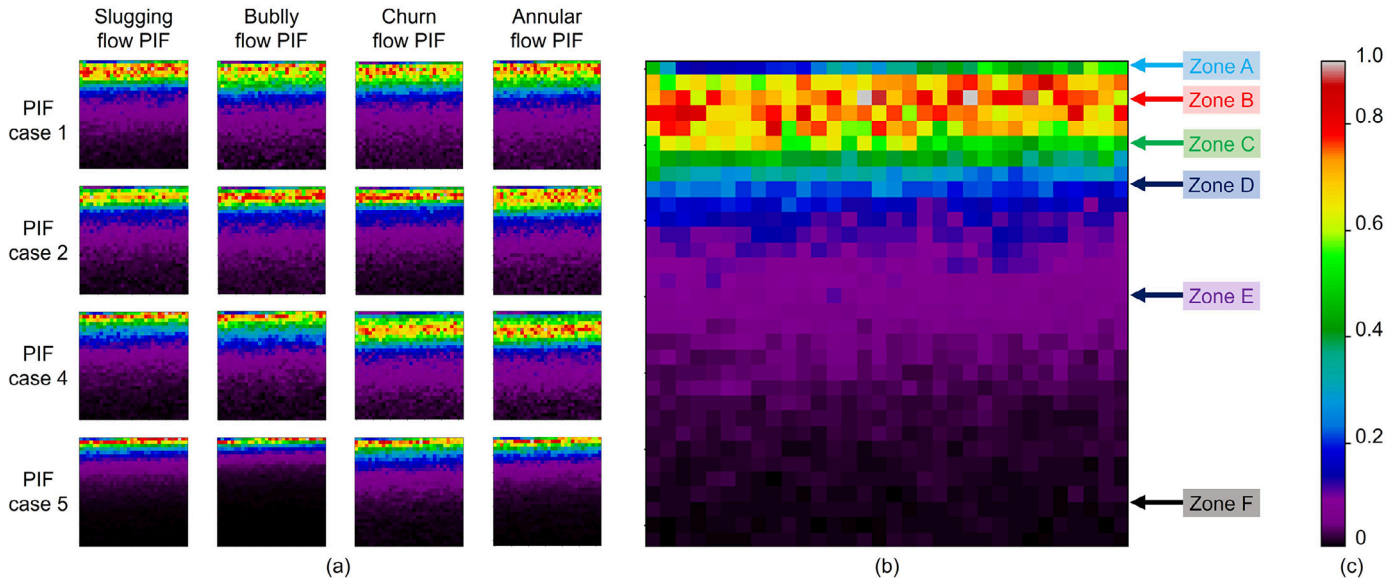

Fig. 7. The PIFs of the flow regimes using the PIF extraction algorithm. All displayed PIFs have been reshaped to the proper size for illumination in the paper. (a) shows the random-selected PIF cases among all four flow regimes. (b) uses the slugging flow PIF from PIF Case 1 in (a) to illustrate the amplitude distribution in a single PIF. (c) shows the visualization color bar, the "nipy_spectral".

activation layer. The stride length of the even layer is two. The seventh layer has only a convolutional layer and a LeakyReLU activation layer. The last three convolutional layers use the kernel size of one-times-one, and the channels are 2,048, 2,048, and 1,024, respectively.

6. Results and analysis

This research used the following hardware: a Dell workstation with GTX1080 GPU (6 GB graphic memory), i7-7700 CPU, and 32 GB memory. The operating environment was Ubuntu 18.04, CUDA 10.2. The deep learning platform was TensorFlow 2.2 [54]. All pseudo-image visualizations used the nipy_spectral color bar of Matplot library.

6.1. The pseudo-image feature (PIF)

6.1.1. Qualitative results and analysis of the PIF

Fig. 3(d) depicts the spectral distribution of the flow regime signal, with three rows corresponding to three L_{WB}. The amplitude distributions among the three channels follow similar patterns, but small differences also exist. The PIF algorithm encoded these similar patterns and differences using the paralleled channels structure, which solved the average blur problem of the TFE algorithm [24]. The experiments in Tab. 2 also proved that this change significantly improved the accuracy of the flow regime identification. Fig. 3(e) splits the three signal rows in Fig. 3(d) into three channels and reshapes them into the pseudo-image feature on the right side of Fig. 3(e). The middle of Fig. 3(e) depicts the process of combining multiple channels into a pseudo-color image. The numerical process is shown in Eq. (5). To the left of Fig. 3(e) is the eventual PIF.

$$Image_{PIF} = \frac{\sum_{c=0}^{c=N_c} feature_c}{N_c} \tag{5}$$

This research randomly selected four sets of PIF from the four flow regimes in Fig. 7(a). Fig. 7(b) approximately divides the PIF into six graphics zones. Zone A corresponds to a short frequency domain with small amplitudes, which are mostly blue or green. Zone B has varied amplitudes with larger values, which are mostly red or yellow. Zone C shows green. Zone D corresponds to a shorter frequency range, and the amplitude is dark blue. The amplitudes of Zones E and F are smaller and are filled with purple and black. Compared with the original flow regime signals in Fig. 3(a), the PIFs of Fig. 7 have more explicit readability. The PIF assists researchers in visually understanding flow regime signals, which allows more vision-based research to be extended to the field of multiphase flow.

The flow regime ultrasonic signal is a one-dimensional waveform signal with a low signal-to-noise ratio. One of the PIF algorithm's contributions is to map the implicit one-dimensional flow regime ultrasonic signal into the two-dimensional Euclidean space. The four flow regimes can identify through the distribution among Zones A/B/C/D/E/F. Although the PIF algorithm has converted the implicit waveform signal to the graphical signal on the Euclidean space, the combination among all seven zones is still a highly complicated human discrimination mission. Therefore, this paper introduces the fully convolutional network (FCN), which supplies powerful analysis capabilities for Euclidean space (as shown in Fig. 6). The convolutional network is a process of removing invalid information and inheriting valid information. After the first convolution block, Zone F of the slugging flow PIF is enlarged, Zone F of the bubbly flow PIF almost disappears, and Zone D is slightly expanded. The chum flow's Zone F narrows, Zone D is substantially broadened, and Zone B is narrowed. Zone D of the annular flow PIF is narrowed, and Zone B almost disappears. This trend is further amplified after the second convolution block, and the chum flow PIF signal is identified (dark blue). In the third convolution block, the slugging flow PIF is also clearly identified (orange). The fourth convolution block distinguishes the bubbly flow PIF (purple). This process reflects the powerful analysis capabilities of convolutional networks based on deep learning for complex signals.

Table 3 illustrates the results of the PIF hyper-parameter test in Table 2. The dataset used in this research consists of two lists, each element in the first list (the input list) containing a single training sample (PIF), and each element in the second list (the output list) containing a single label. It is clear that the input list elements and the output list elements are in one-to-one correspondence, and the lengths of the two lists are equal. To overcome the categorical bias, this study first conducted a random shuffle of the dataset. It then divided the dataset using a ratio of 6 to 2 to 2. Sixty percent of the data formed the training set, while 20% of the data formed the testing set, which cross-validated the overfitting or underfitting level. The remaining data formed the validation set. The validation set did not participate in the training process, which validated the model's performance when it stopped training. It is worth noting that the flow labels encoded with the one-hot form, which trans-

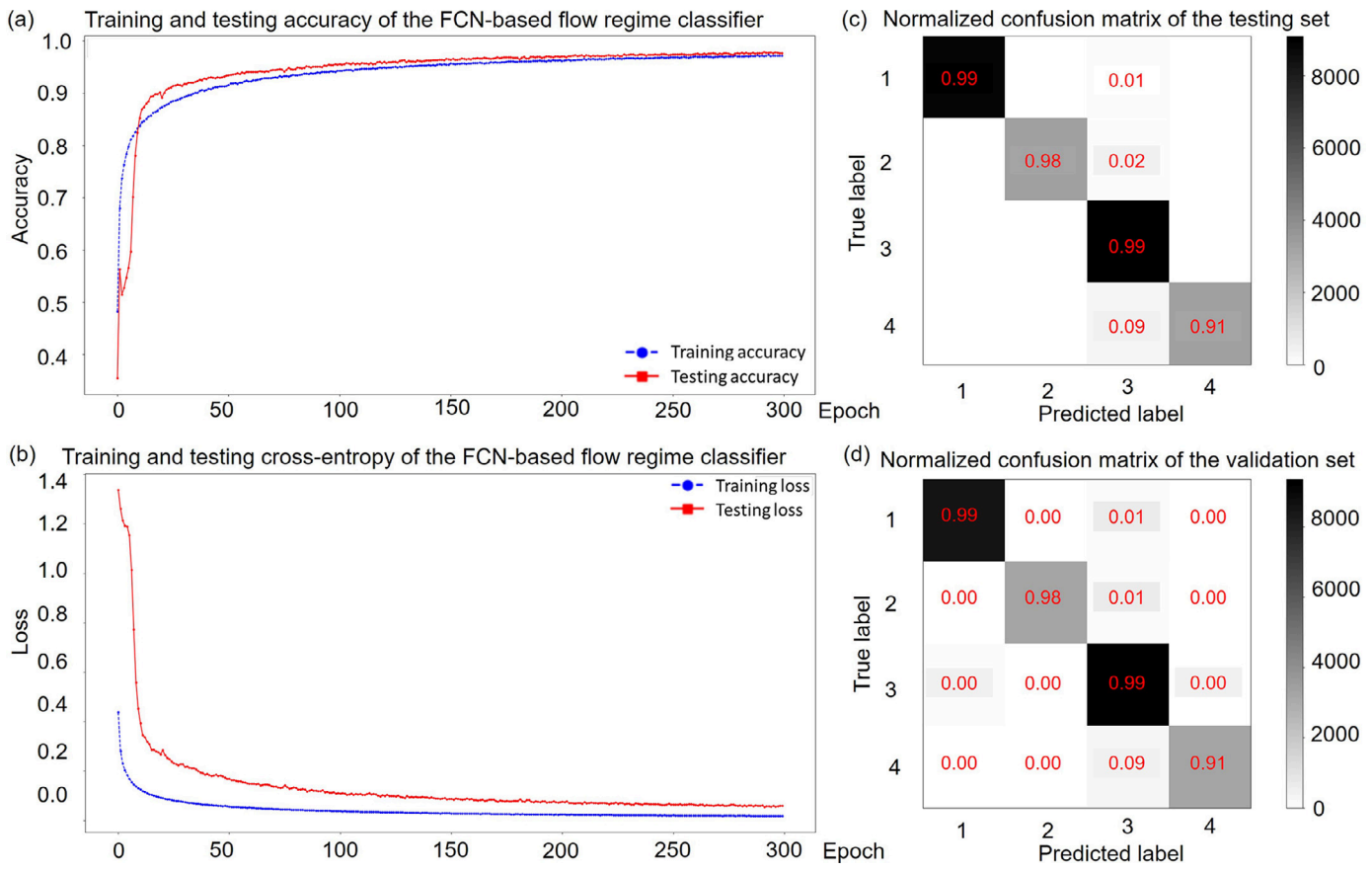

Fig. 8. The quantitative result of Experiment 21 in Tab. 2. (The benchmark of the proposed DNN flow regime classifier in Section 5.1.)

formed multi-classification into four binary classifications. The one-hot label was able to avoid the gradient blur from the intermediate values, so the classifier was easier to converge. The shuffled flow regime dataset was divided into training, testing, and validation sets according to a 60%/20%/20% ratio. "cb" refers to the call-back setting, which is either the converge point or the fixed training epoch value. The learning rate was 0.00001, the batch size was 1024 samples, the loss was categorical cross-entropy, and the metric used accuracy and mean square error (MSE).

6.1.2. *Quantitative results and analysis of the PIF experiments*

This research compared all 20 experimental results with the state-of-the-art [24]. Notably, this research utilized the same data as that used by Nnabuife et al. [24], which makes the results more convincing and comparable. This section focuses on an illustration and explanation of the results, while a more detailed cross-comparison is discussed in Section 6.1.3.

The four essential indexes for evaluating the deep learning classification model are accuracy trend curves, loss trend curves, the testing confusion matrix, and validation confusion matrix. It is critical to display all 20 experimental results completely and credibly. Thus, all the experimental results are presented at the end of Section 6.1.3 (Fig. 11-30). Each experimental result is divided into (a) (b) (c) and (d) subfigures, which correspond to the four essential indexes.

The two significant challenges of deep learning models are underfitting and overfitting. This research uses the accuracy trend curve and the loss trend curve to evaluate the models. Both accuracy and loss are global indicators. The confusion matrix of the testing set and validation set display the model's classification results for each flow regime in detail. The accuracy trend curve represents the overall performance of the proposed model on multi-classification problems. It can be further divided into training accuracy trend curves (blue curves) and testing accuracy trend curves (red curves). An increase in training accuracy indicates that the model is still learning on the training set; otherwise, it indicates that the model is overfitting. An increase in validation accuracy indicates an increase in the model's generalization ability; otherwise, the generalization ability decreases, and the model is underfitting. When the accuracy curves are insufficient to represent the model's status, the loss curves can reveal more information. The loss trend curves can also be divided into training loss trend line (red curves) and testing loss trend line (blue curves). A decrease in training and testing loss indicates that the model is still learning; otherwise, the model is overfitting.

The gray-scale color used in the confusion matrix represents the absolute number of samples corresponding to each category, and the color bar is displayed on the right. The red number represents the corresponding accuracy value, which is a relative value. The vertical axis refers to the ground-truth labels (corresponding to True and False labels). The horizontal axis refers to the predicted labels (corresponding to the Positive and Negative predictions). The confusion matrix's diagonal blocks represent the True-Positive value, the upper-right blocks represent the False-Positive value, and the lower-left blocks represent the True-Negative value. Ideally, the deeper the diagonal blocks' grayscales are, and the larger the diagonal blocks' accuracy values are, the better the result.

Fig. 11 presents the results of Experiment 1 (Table 2). The DNN classifier converged in about 100 epochs, then entered the overfitting state. The training curves (Fig. 11[a] and [b]) were relatively smooth, which indicates that the model was relatively stable. The confusion matrix (Fig. 11[c] and [d]) indicates that Experiment 1 demonstrated insufficient ability in recognizing slugging, churn, and annular flow regimes, which shows lower performance than Nnabuife et al. [24].

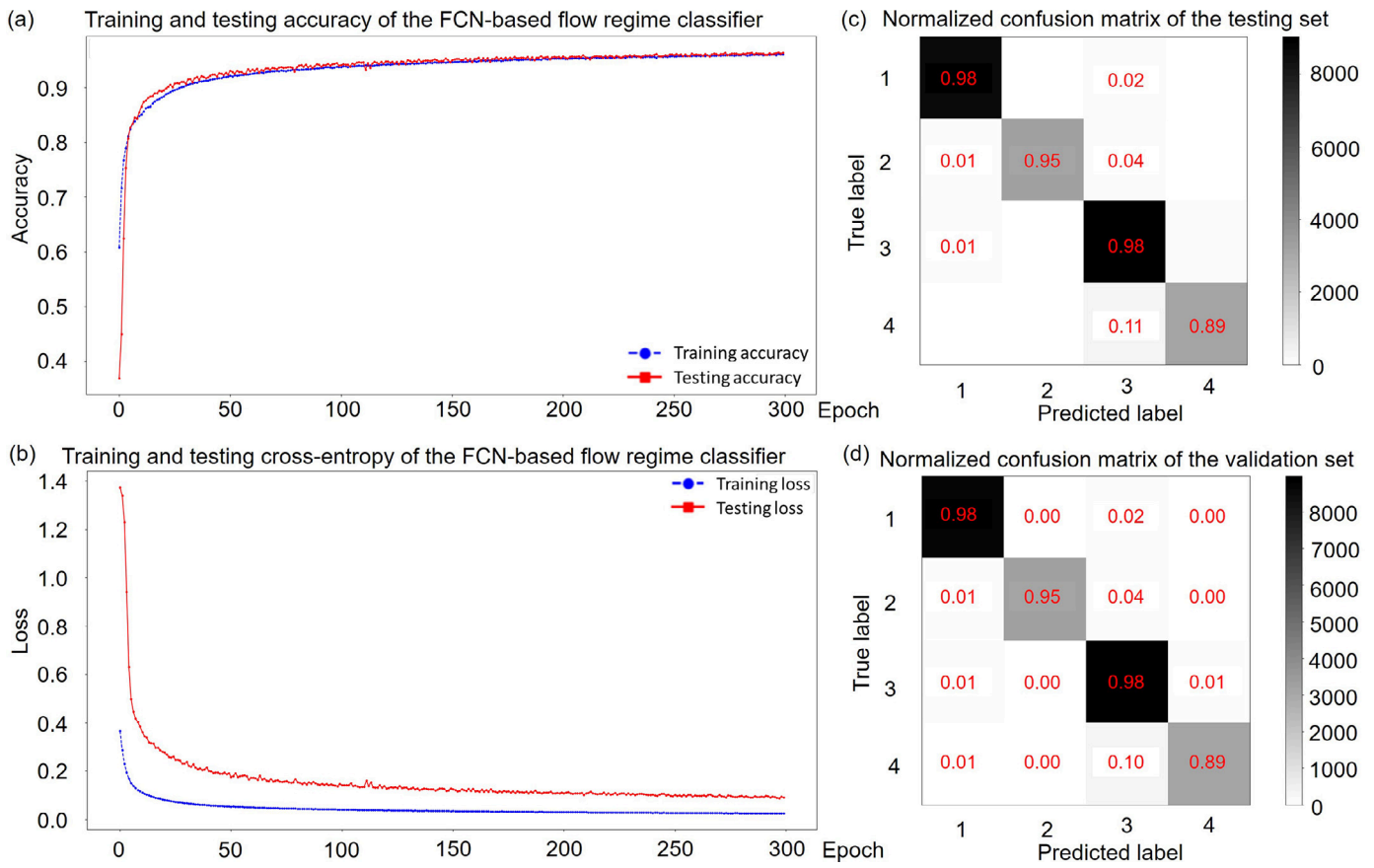

Fig. 9. The benchmark of the proposed CNN flow regime classifier in Section 5.2.

Fig. 12 presents the results of Experiment 2 (Table 2). The DNN classifier converged in about 80 epochs, and the subsequent overfitting degree was less than in Experiment 1. The training curves (Fig. 12[a] and [b]) were also very smooth. The confusion matrix (Fig. 12[c] and [d]) indicates that although Experiment 2 did not demonstrate better performance than Nnabuife et al. [24], it achieved better results than Experiment 1. It is noteworthy that Experiment 2 improved the final result of the model while reducing the difficulty of convergence.

Fig. 13 presents the results of Experiment 3 (Table 2). The DNN classifier converged in about 600 epochs. Although Experiment 3 improved the performance of the PIF, the learning difficulty increased (more epochs were needed to achieve convergence). Experiment 3 reduced the degree of overfitting, and the curves became more smooth (Fig. 13[a] and [b]). The confusion matrix (Fig. 13[c] and [d]) indicates that the performance of Experiment 3 was still lower than Nnabuife et al. [24].

Fig. 14 presents the results of Experiment 4 (Table 2). The DNN classifier converged in about 400 epochs. The confusion matrix (Fig. 14[c] and [d]) indicates that Experiment 4 achieved comparable results to Nnabuife et al. [24].

Fig. 15 presents the results of Experiment 5 (Table 2). The DNN classifier converged in approximately 60 epochs. However, the accuracy only attached around 87%, and then the model was over-fitted. This result illustrates that the PIF from Experiment 5 lost too much valid information for the classification mission. The confusion matrix (Fig. 15[c] and [d]) illustrates that the performance of Experiment 5 was lower than Nnabuife et al. [24].

Fig. 16 presents the results of Experiment 6 (Table 2). The DNN classifier converged in about 300 epochs. The confusion matrix (Fig. 16[c] and [d]) show that Experiment 6 demonstrates relatively good performance. But it was not better than Nnabuife et al. [24].

Fig. 17 presents the results of Experiment 7 (Table 2). The DNN classifier converged in about 200 epochs. The confusion matrix (Fig. 17[c] and [d]) indicates that Experiment 7 had a far better performance than Nnabuife et al. [24]. However, the PIF dimension from Experiment 7 was also much larger than Nnabuife et al. [24]. One purpose of this research was to explore a more compact flow regime coding method. Although Experiment 7 achieved outstanding flow regime classification performance, subsequent experiments further explored more excellent PIF hyperparameter design schemes.

Fig. 18 presents the results of Experiment 8 (Table 2). The DNN classifier converged in about 120 epochs. The confusion matrix (Fig. 18[c] and [d]) illustrates that Experiment 8 achieved better performance than Nnabuife et al. [24] but slightly lower than Experiment 7.

Fig. 19 presents the results of Experiment 9 (Table 2). The DNN classifier converged in approximately 150 epochs. The confusion matrix (Fig. 19[c] and [d]) illustrates that the performance in Experiment 9 was lower than Nnabuife et al. [24] Experiment 9 not only increased the convergence time but also reduced the performance of flow regime identification.

Fig. 20 presents the results of Experiment 10 (Table 2). The DNN classifier converged in about 100 epochs. The performance in Experiment 10 was lower than Nnabuife et al. [24], and the PIF from Experiment 10 lost too much valid information for the classification mission.

Fig. 21 presents the results of Experiment 11 (Table 2). The DNN classifier converged in about 500 epochs. The confusion matrix (Fig. 21[c] and [d]) shows that Experiment 11 had far better performance than Experiment 7 and Nnabuife et al. [24]. Experiments 12, 13 and 14 further tested the influence of N_{fft} on PIF performance. Fig. 22 presents the results of Experiment 12 (Table 2). The DNN classifier converged in about 100 epochs. Compared to Experiment 11, the accuracy of testing and verification dropped by about 2%. Fig. 23 presents the results

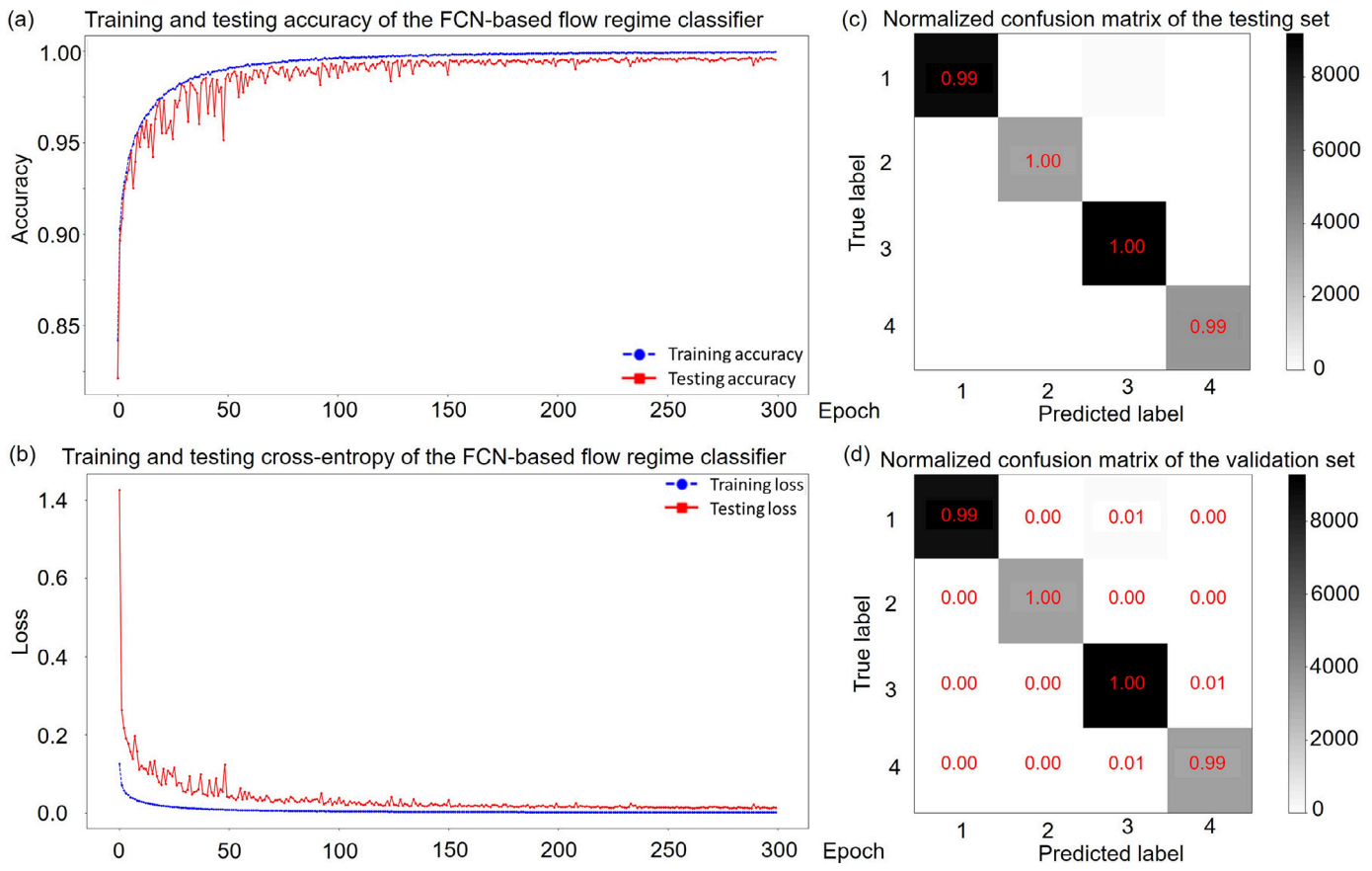

Fig. 10. The benchmark of the proposed-FCN flow regime classifier in Section 5.3.

of Experiment 13 (Tab. 2). The DNN classifier converged in about 80 epochs. Compared with Experiment 11, the accuracy of testing and verification was reduced by 6%. Fig. 24 presents the results of Experiment 14 (Table 2). The DNN classifier converged in approximately 60 epochs. Compared with Experiment 11, the training accuracy decreased by 9%, and the testing and verification accuracy dropped by nearly 10%. Overall, Experiments 11, 12, 13, and 14 demonstrated that PIF performance was negatively correlated with the value of N_{fft}.

Fig. 25 presents the results of Experiment 15 (Table 2). The DNN classifier converged in about 150 epochs. Both the testing and verification accuracy achieved far better performance than Nnabuife et al. [24], which shows the state-of-the-art flow regime performance.

Fig. 26 presents the results of Experiment 16 (Table 2). The DNN classifier converged in about 40 epochs. The confusion matrix (Fig. 26[c] and [d]) indicates that the PIF from Experiment 16 decreased the flow regime performance.

Fig. 27 presents the results of Experiment 17 (Table 2). The DNN classifier converged in approximately 90 epochs. The confusion matrix (Fig. 27[c] and [d]) illustrates that Experiment 17 also achieved performance far better than Nnabuife et al. [24].

Fig. 28 presents the results of Experiment 18 (Table 2). The DNN classifier converged in about 400 epochs. However, the confusion matrix (Fig. 28[c] and [d]) illustrates that the performance of Experiment 18 is lower than that of Nnabuife et al. [24].

Fig. 29 presents the results of Experiment 19 (Table 2). The DNN classifier converged in about 180 epochs. The confusion matrix (Fig. 29[c] and [d]) illustrates that Experiment 19 has achieved far better performance than Nnabuife et al. [24].

Fig. 30 presents the results of Experiment 20 (Table 2). The DNN classifier converged in about 100 epochs. The confusion matrix (Fig. 30[c] and [d]) illustrates that Experiment 20 not only improved the convergence efficiency but also dramatically improved the identification performance of the flow regime.

6.1.3. Cross-comparison of the PIF experiments

The control variable of Experiments 1, 2, 3, and 4 was N_{WB} (or the length of S_{WB}). Experiment 4 had the highest testing and validation accuracy, Experiment 1 had the lowest, and Experiments 2 and 3 had similar results. This suggests that increasing the number of N_{wb} can improve the performance of the PIF. Fast-Fourier transform exhibits amplitude leakage at the head and tail of the input signal, and the method of averaging multiple window B can reduce the leakage level.

The control variable of Experiments 3, 5, 6, 7, 11, and 13 was the $N_{channel}$. These experiments can be divided into three groups according to L_{WA} (Group 1: 3 and 5; Group 2: 6 and 13; Group 3: 7 and 11). It is clear that the accuracy of the three groups did not change much. However, compared with the results of TFE [24], the accuracy of Experiment 11 was greatly improved. It is worth noting that only increasing the number of $N_{channel}$ did not improve the PIF performance, but more than one $N_{channel}$ improved the accuracy.

The control variable of Experiments 7, 8, 9, 10, 11, 12, 13, and 14 was N_{fft}. They can be divided into two groups according to different N_{LWB} (Group 1: 7, 8, 9, and 10; Group 2: 11, 12, 13, and 14). The accuracy of testing and validation in both groups increased as N_{fft} increased. However, the N_{fft} increase also made the PIF size increase, which increased the cost of computational consumption. Therefore, balancing the amount of calculation and accuracy is a particularly important task for the PIF algorithm.

The control variable of Experiments 2, 3, 5, 6, 15, 16, and 17 was L_{WA}. They can be divided into three groups (Group 1: 2 and 3; Group 2: 5 and 6; Group 3: 15, 16, and 17). The performance of the PIF increased as the L_{WA} increased.

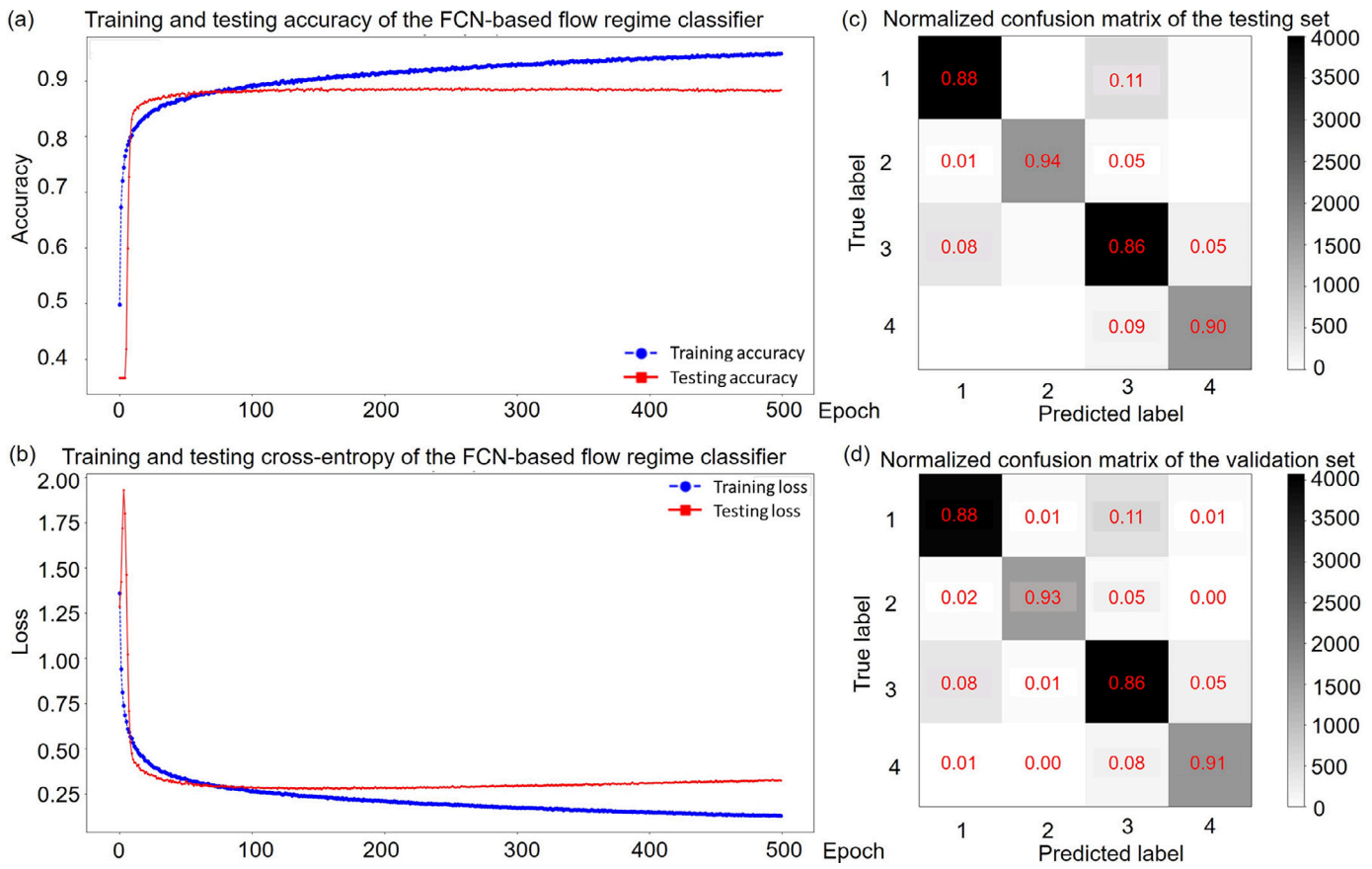

Fig. 11. The quantitative results of Experiment 1 in Tab. 2. (a) and (b) respectively refer to the training/testing accuracy and loss of Experiment 1. (c) and (d) refer to the confusion matrix of the testing and validation sets, respectively. To the right of both (c) and (d) is the color bar for indexing the sample amount of the corresponding set, the unit being samples.

The control variable of Experiment 11, 18, and 19 was S_{WA} (or N_{PIF}). It is clear that the accuracy of testing and validation was greatly improved as S_{WA} decreased.

The control variables of Experiments 19, 20, and 21 were height (h) and width (w) in two-dimensional space. The h in the first 19 experiments was equal to one, and the best result was found in Experiment 19. Experiment 20 compressed the spectrum of three channels into one channel, and Experiment 21 transformed it into 32*32*3 in two dimensions. The results revealed that the 2D reshape did not affect the accuracy of the DNN classifier. However, the result of Experiment 21 was more similar to the image format, which was more in line with the goal of explicitly displaying the flow regime features. Therefore, this study uses the PIF hyper-parameters of Experiment 21 as the recommended parameters.

6.2. Flow regime classifiers and benchmarks

This section focuses on the performance of different classifiers. The benchmarks of different deep learning classifiers for flow regime identification are shown in Table 3. All experiments used the same training hyper-parameters as listed in Section 6.1. The three classifiers were superior to the existing models in testing and verification accuracy and MSE. Only ResNet and DenseNet demonstrated acceptable results. However, ResNet and DenseNet both reached 100% training accuracy prematurely, which decreased the learning ability of the classifier. ResNet and DenseNet have good learning capabilities, especially for complex situations with large amounts of data. However, traditional engineering research including flow regime identification does not have a large amount of data, which makes the learning performance of the custom small classifier even more remarkable.

In the last two rows of Table 4, there are two more results. Nnabuife et al. [55] used PCA and SVM to achieve a classification accuracy of 84.6%. Nnabuife et al. [24] further achieved 96.35% accuracy in testing set using TFE and DNN. However, The TFE+DNN classifier took 1,300 epochs. Experiments 19 and 20 in Table 2 obtained 99.56% accuracy in 500 epochs. This demonstrates that PIF has much better performance than TFE.

This section's focus is to propose a fair flow regime identification benchmark, rather than to achieve the best identification accuracy (in fact, Section 6.1 has achieved various sufficient identification results). Therefore, the results in Table 4 are not necessarily better than in Table 3. The benchmark proposed in this paper uniformly uses 300 training epochs.

Fig. 8 illustrates the performance of the proposed DNN-based flow regime classifier in the benchmark setting.

Fig. 9 shows the performance of the proposed CNN classifier in the benchmark setting. Fig. 9(a) and (b) depict a fantastic learning curve, and the model was very stable. After 300 epochs, the proposed DNN flow state classifier had surpassed Nnabuife et al. [24].

Fig. 10 illustrates the performance of the proposed FCN classifier in the benchmark setting. Fig. 10(a) and (b) show that the model had a certain degree of unstable oscillation before 150 epochs, and then the area was stable. However, the verification and test accuracy were higher than the training accuracy, which suggests that the model is still in a promising learning stage, and extending the number of learning epochs can improve the FCN network's performance. The FCN network has achieved a good learning result while using a smaller-scale calculation graph.

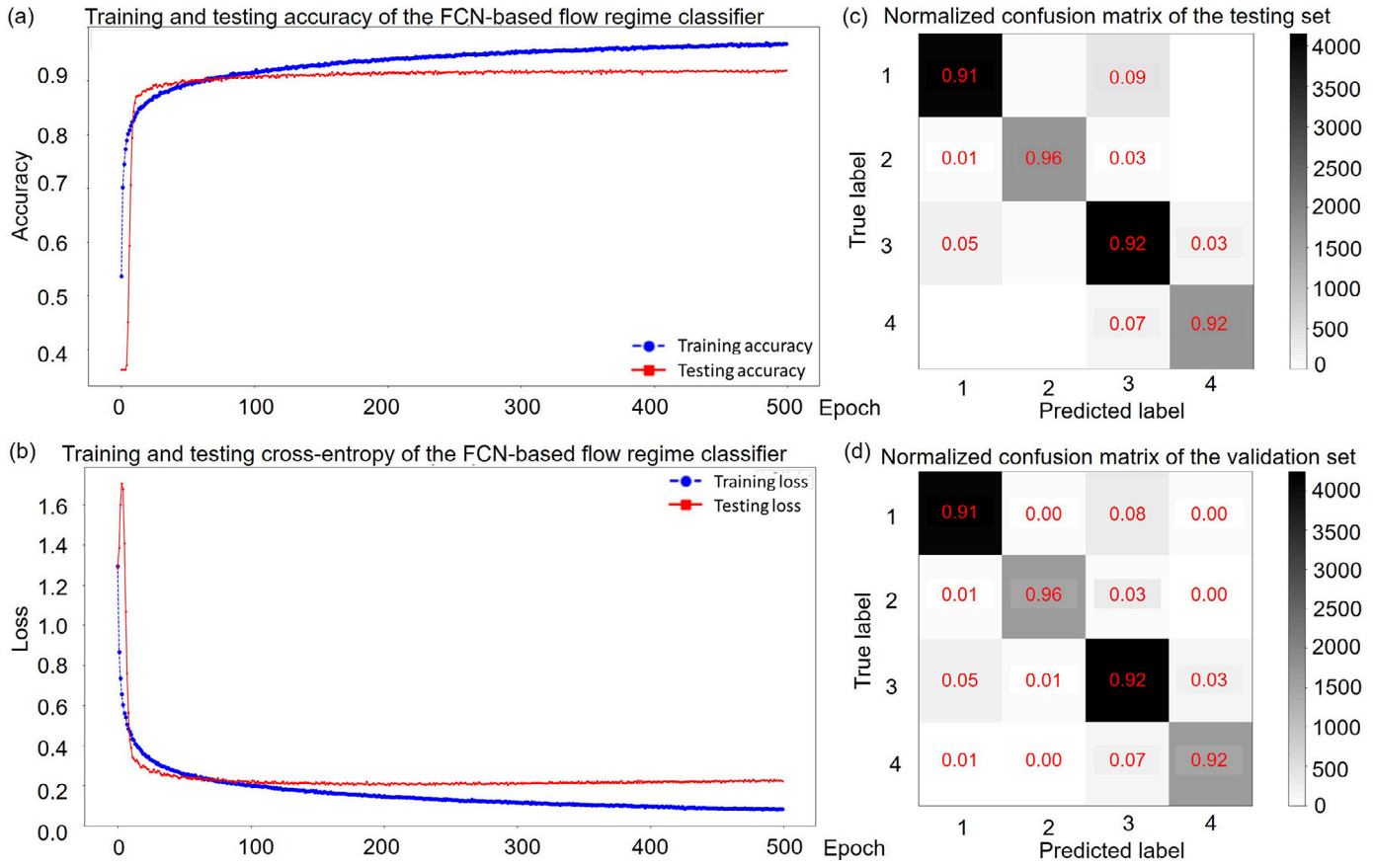

Fig. 12. The quantitative results of Experiment 2 in Tab. 1.

Tab. 4
The proposed flow regime identification benchmark. The red values refer to the best classifier. The bold values represent the best value among all classifiers, and the "/" refers to a non-applicable item. The existing popular classifiers are VGG [34], ResNet [35], DenseNet [36], MobileNet [37], and NASNet [38].

	$loss_{train}$			$loss_{test}$			$loss_{valid}$				
Classifier	acc_{train}(%)	cce	mse	acc_{test}(%)	cce	mse	acc_{valid}(%)	cce	mse	cb(epoch)	lr
DNN	97.20	0.0180	0.0104	97.66	0.0599	0.0087	97.77	0.0553	0.0081	300	0.00001
CNN	95.96	0.1250	0.0145	96.26	0.0903	0.0132	96.42	0.0887	0.0128	300	0.00001
FCN	99.95	0.0013	3.9175*e-4	**99.95**	**0.0141**	**0.0019**	**99.54**	**0.0132**	**0.0017**	300	0.00001
VGG19	36.92	0.3228	0.1810	36.80	1.3614	0.1808	36.45	1.3632	0.1811	300	0.00001
Pre+VGG19	36.76	0.3230	0.1811	36.69	1.3602	0.1808	37.03	1.3552	0.1803	300	0.00001
ResNet50	**100.0**	**2.0545xe-4**	**8.9603*e-6**	90.53	0.3879	0.0391	90.38	0.3908	0.0396	300	0.00001
DenseNet121	99.99	5.6583xe-4	7.1905*e-5	96.09	0.1341	0.0155	96.20	0.1292	0.0152	300	0.00001
MobileNetv2	97.38	0.0166	0.0102	77.18	0.9531	0.0938	77.71	0.9507	0.0918	300	0.00001
Pre+MobileNetv2	99.81	0.0018	8.4910*e-4	33.70	9.5438	0.3570	35.09	9.5601	0.3213	300	0.00001
NASNetMobile	99.83	0.0021	8.5699*e-4	13.38	72.7383	0.4331	13.58	72.5081	0.4321	300	0.00001
PCA+SVM	85.7	/	/	84.6	/	/	/	/	/	/	/
TFE+DNN	99.01	/	0.0060	96.28	/	0.0152	96.35	/	0.0159	1300	0.00001

The following results illustrate the difficulty of directly using existing deep learning architectures in flow regime identification, which is a current popular topic called transfer learning. They also highlight the significant performance of the proposed flow regime identification model.

Fig. 31 and Fig. 32 illustrate the VGG19 network results and the preprocessing layer connected VGG-19 network. It is clear that directly migrating the VGG network that performed well on ImageNet [56] to flow pattern recognition did not achieve good results. Fig. 33 depicts the performance of the ResNet network. The convergence point of ResNet50 was about 30 epochs, and then it entered overfitting. The final transfer training result was worse than that of Nnabuife et al. [24]. Fig. 34 shows the result of DenseNet121. DenseNet121 converged in about 60 epochs. Compared with ResNet50, DenseNet121 achieved better performance, which was roughly equivalent to Nnabuife et al. [24]. Fig. 35 and Fig. 36 illustrate the performance of MobileNet and preprocessing layer+MobileNet. Neither could meet the needs of flow pattern recognition. Fig. 37 shows the performance of NASNet. The result could not meet the requirements of flow analysis. These results demonstrate that the migration of existing image-based networks to flow pattern recognition is facing significant challenges.

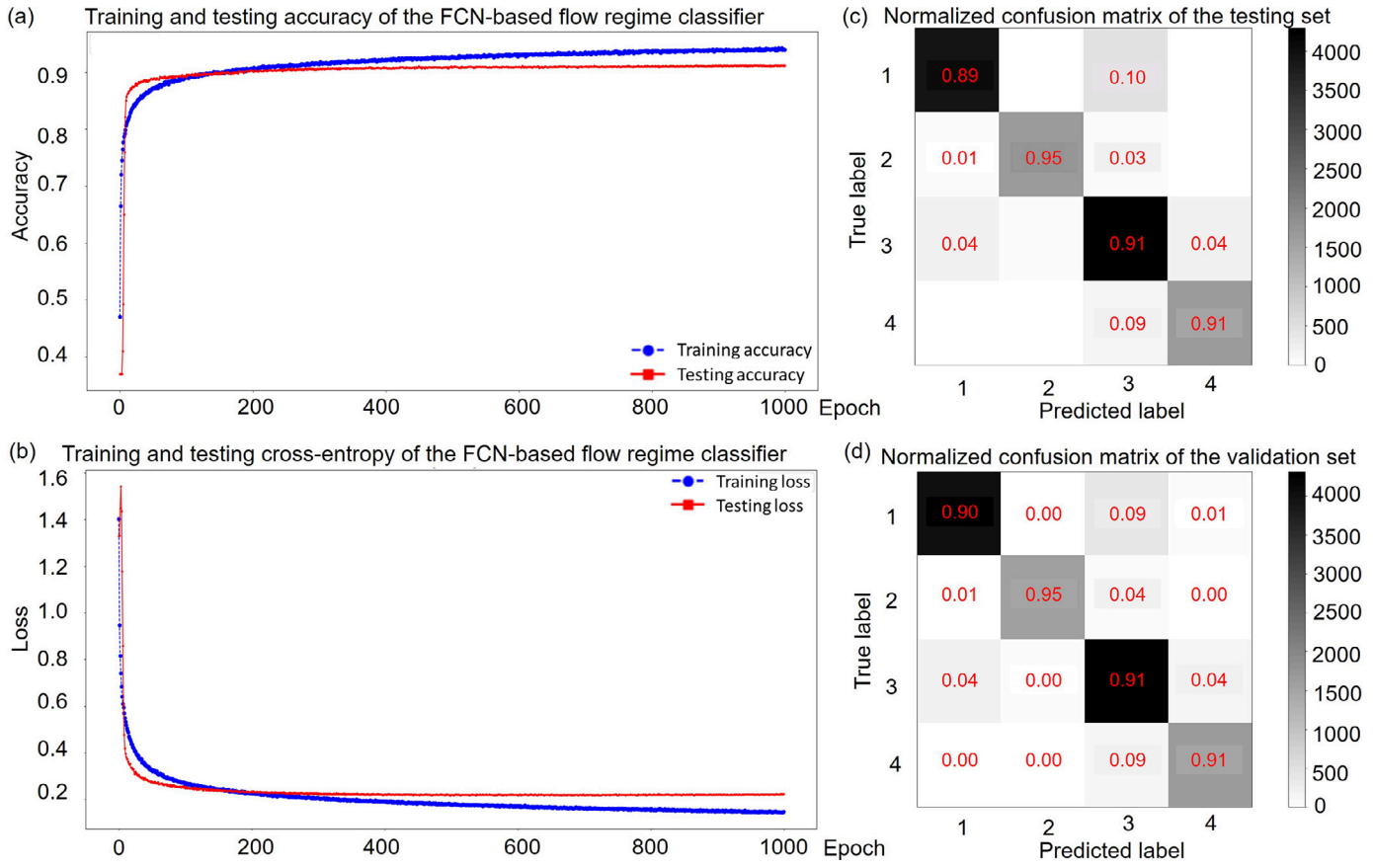

Fig. 13. The quantitative results of Experiment 3 in Tab. 2.

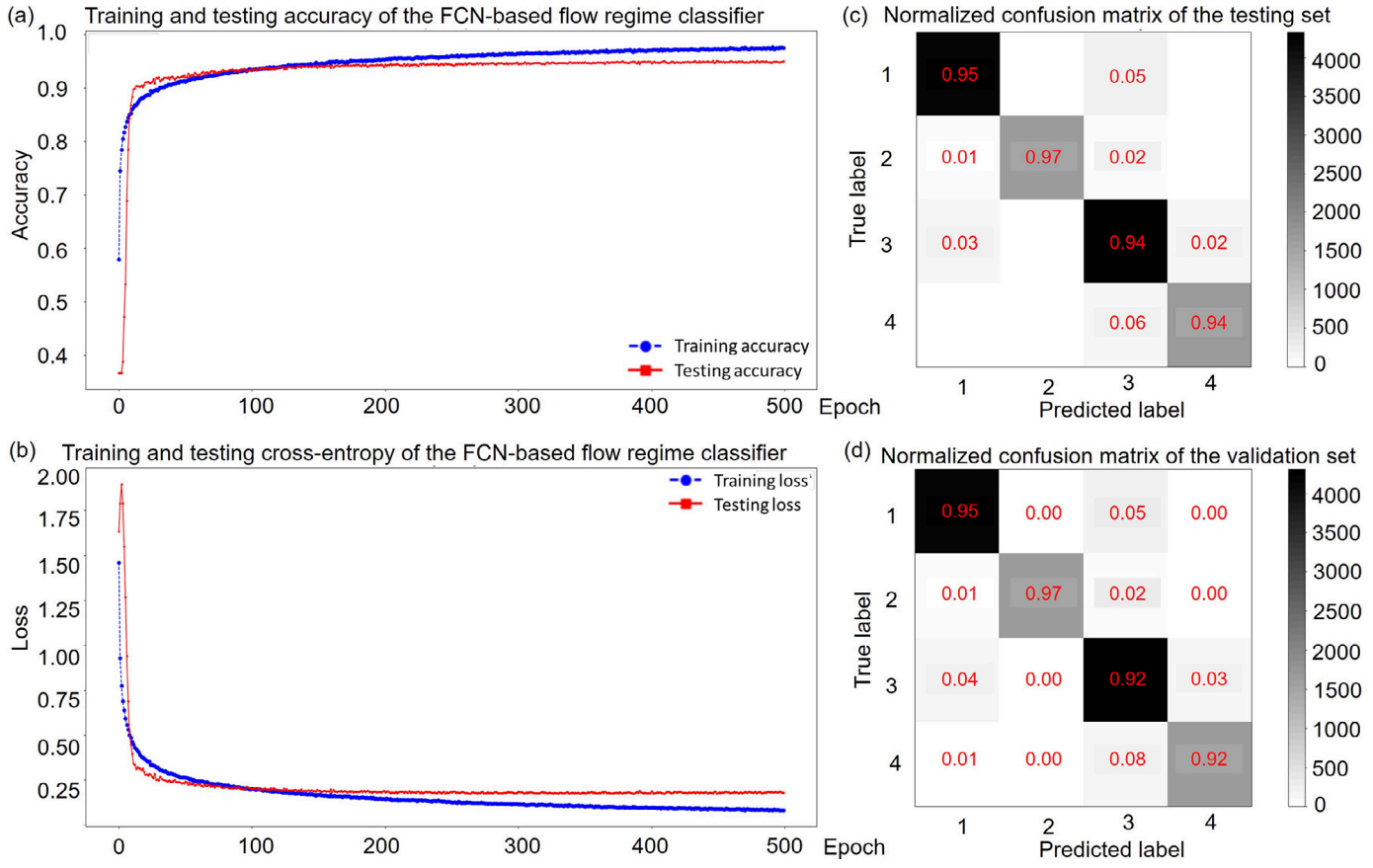

Fig. 14. The quantitative results of Experiment 4 in Tab. 2.

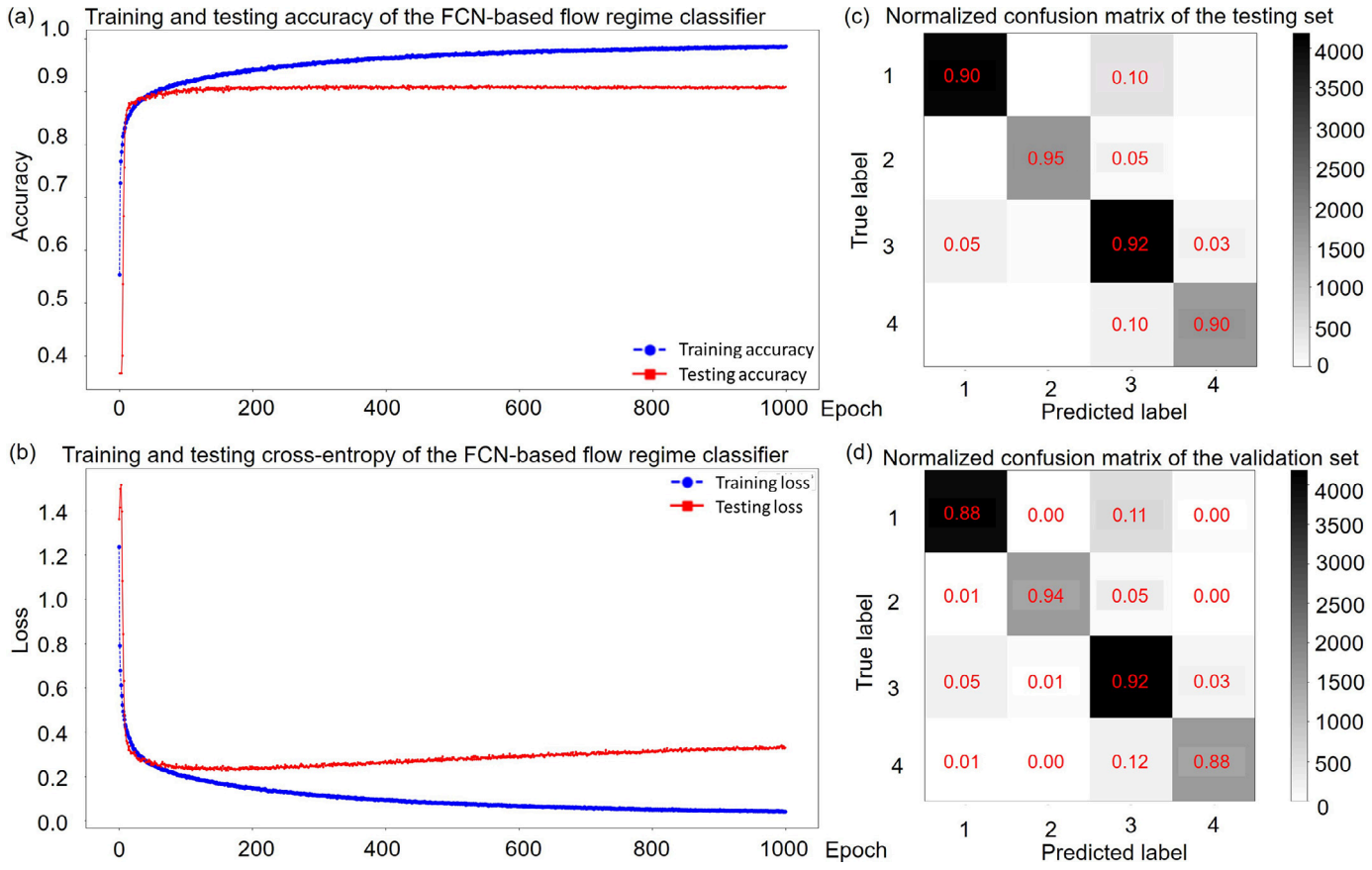

Fig. 15. The quantitative results of Experiment 5 in Tab. 2.

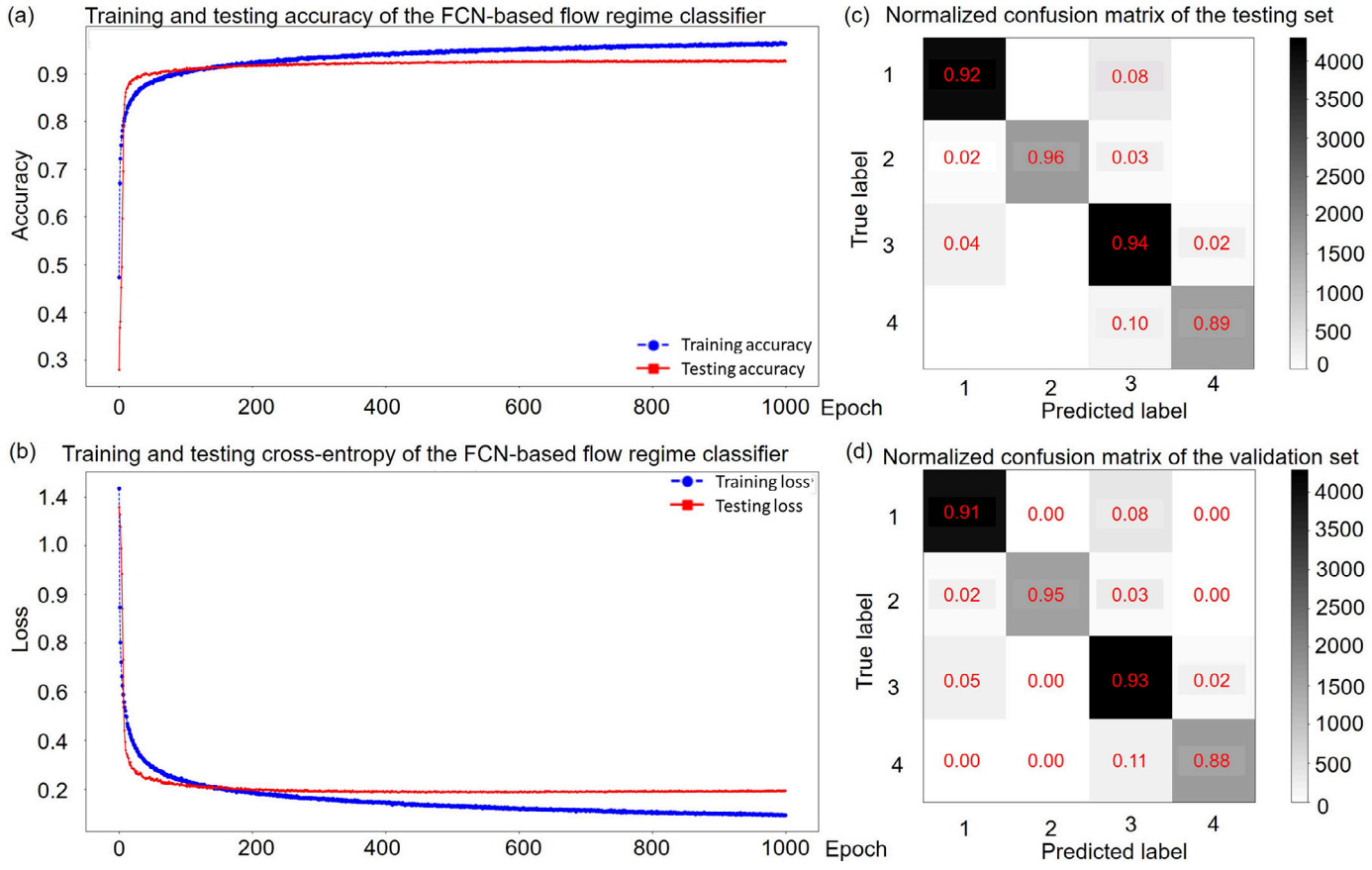

Fig. 16. The quantitative results of Experiment 6 in Tab. 2.

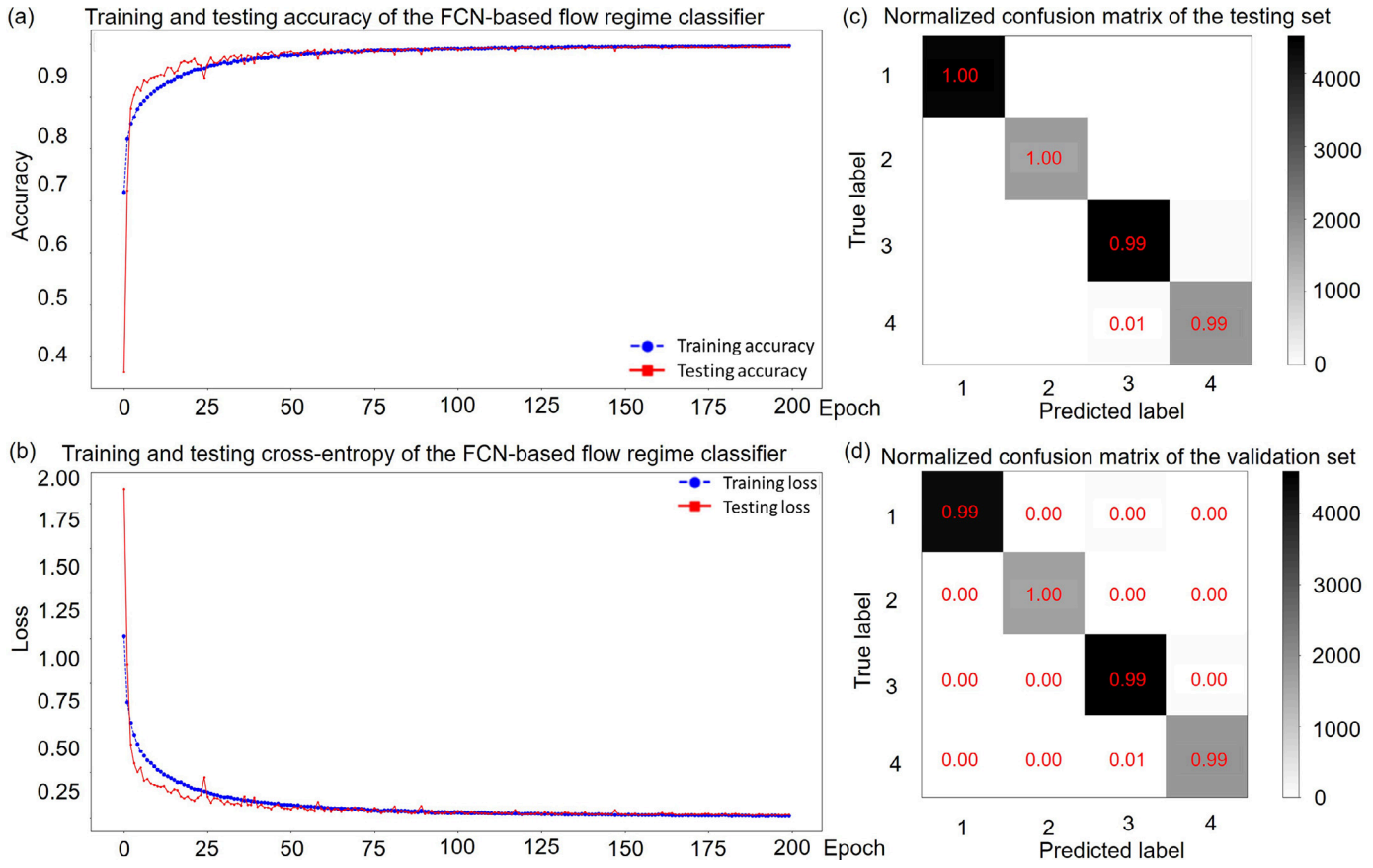

Fig. 17. The quantitative results of Experiment 7 in Tab. 2.

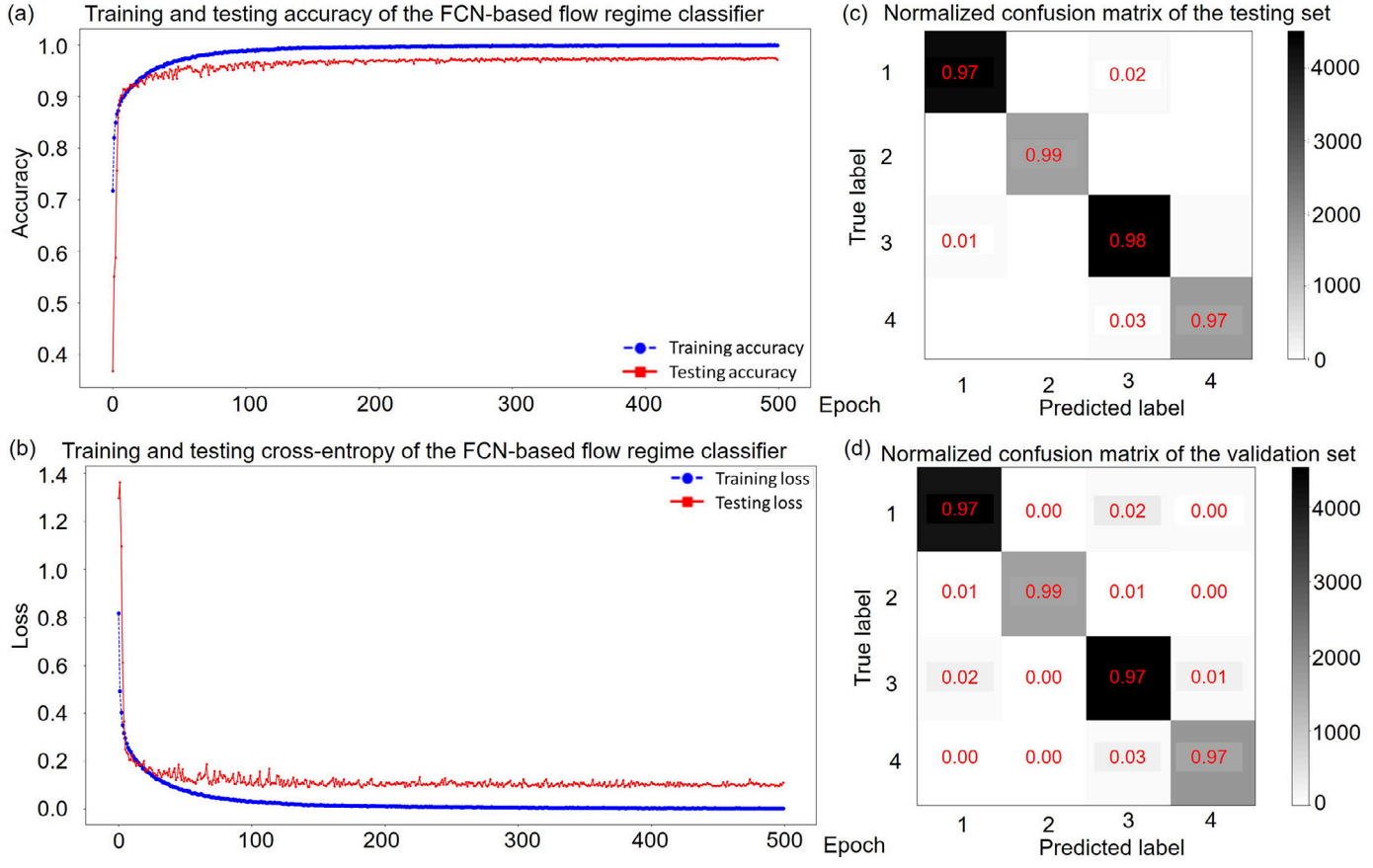

Fig. 18. The quantitative results of Experiment 8 in Tab. 2.

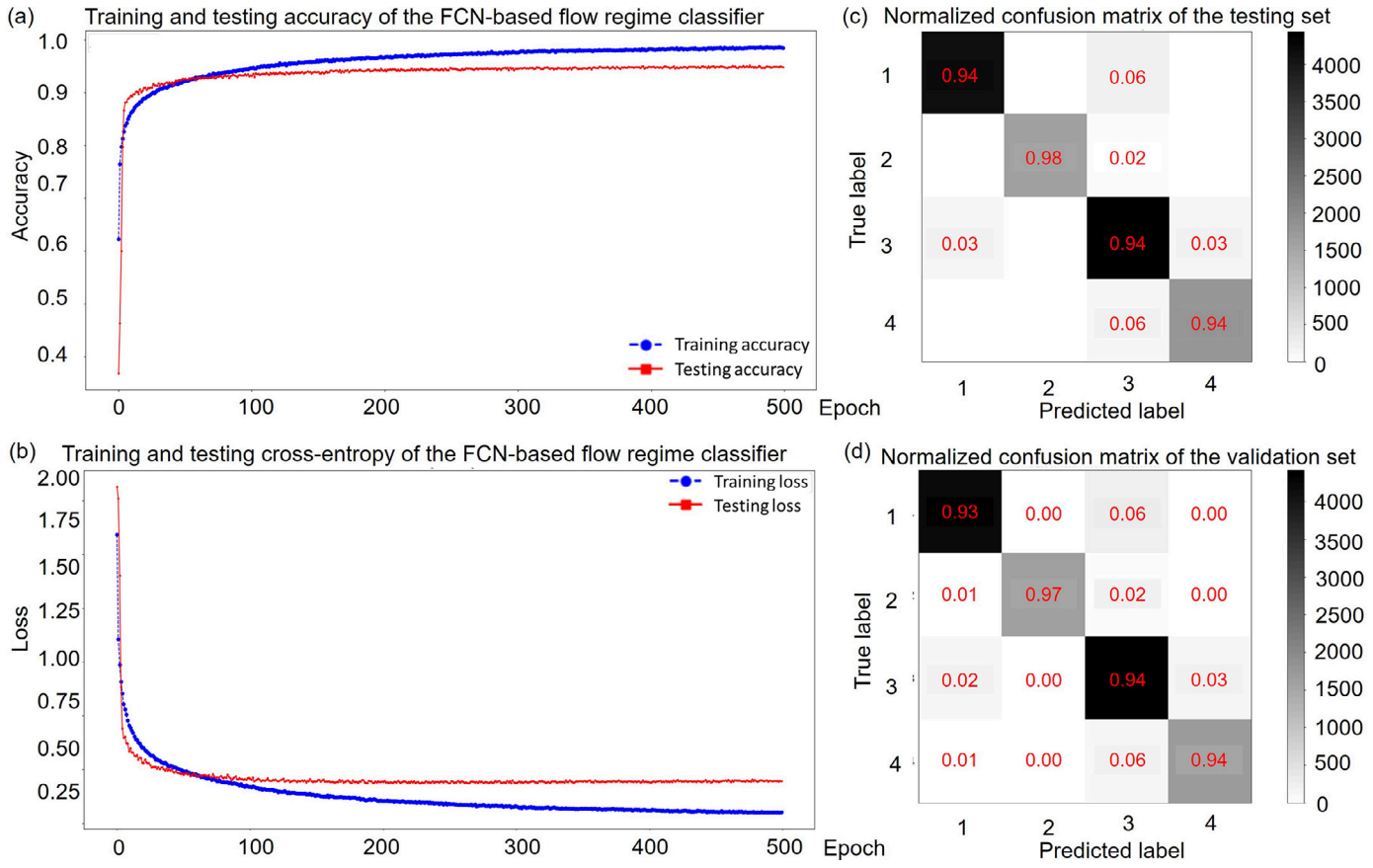

Fig. 19. The quantitative results of Experiment 9 in Tab. 2.

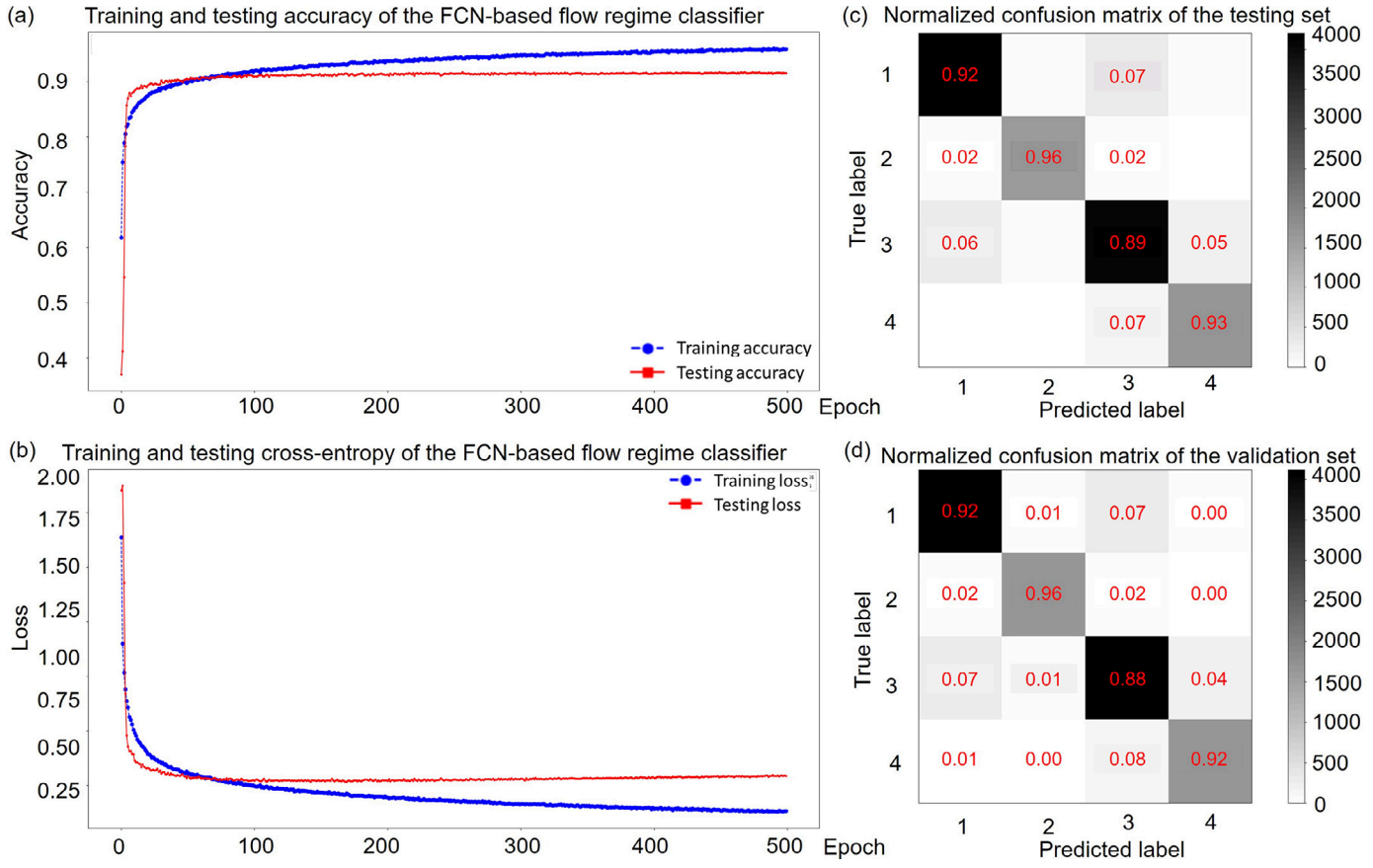

Fig. 20. The quantitative results of Experiment 10 in Tab. 2.

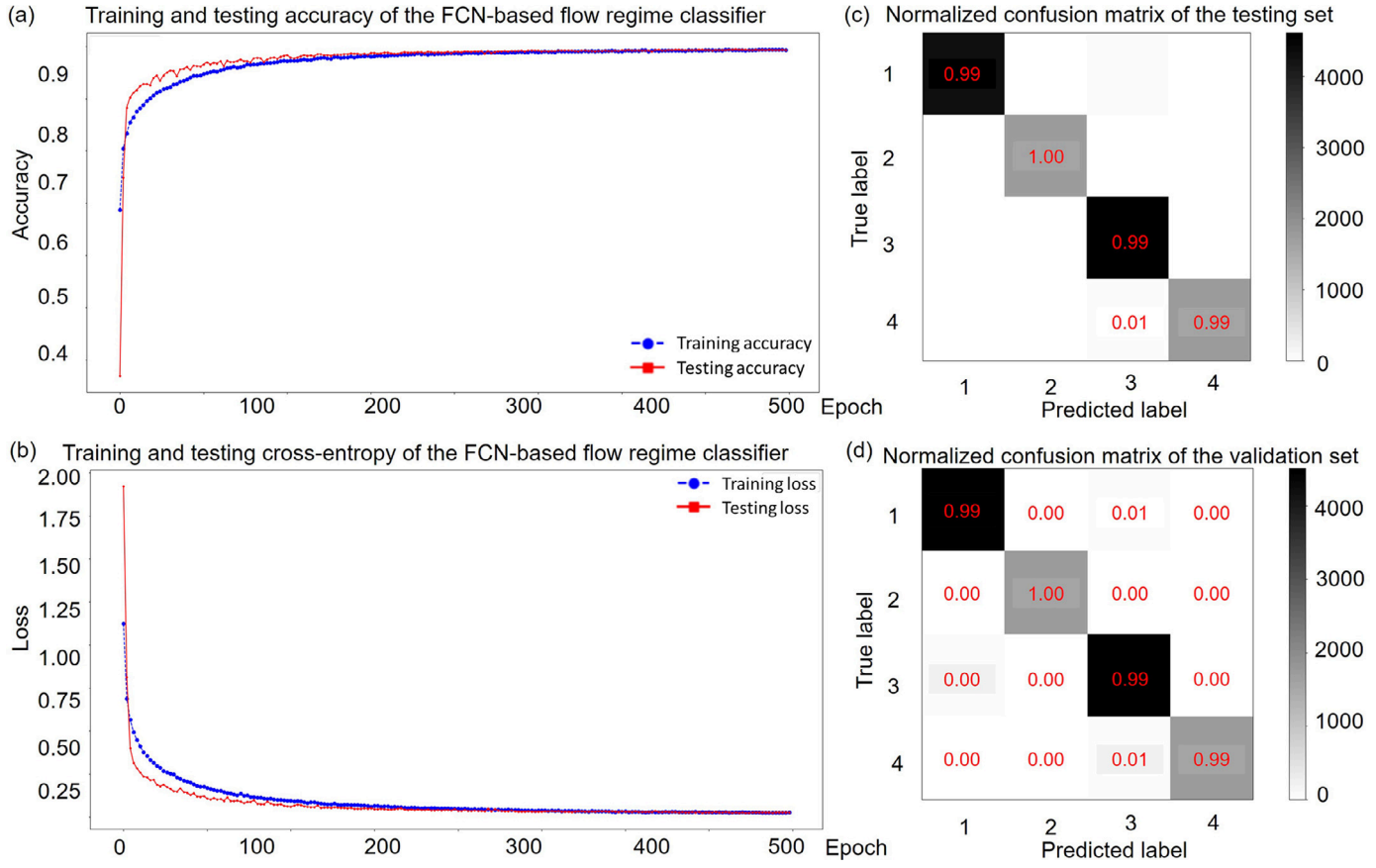

Fig. 21. The quantitative results of Experiment 11 in Tab. 2.

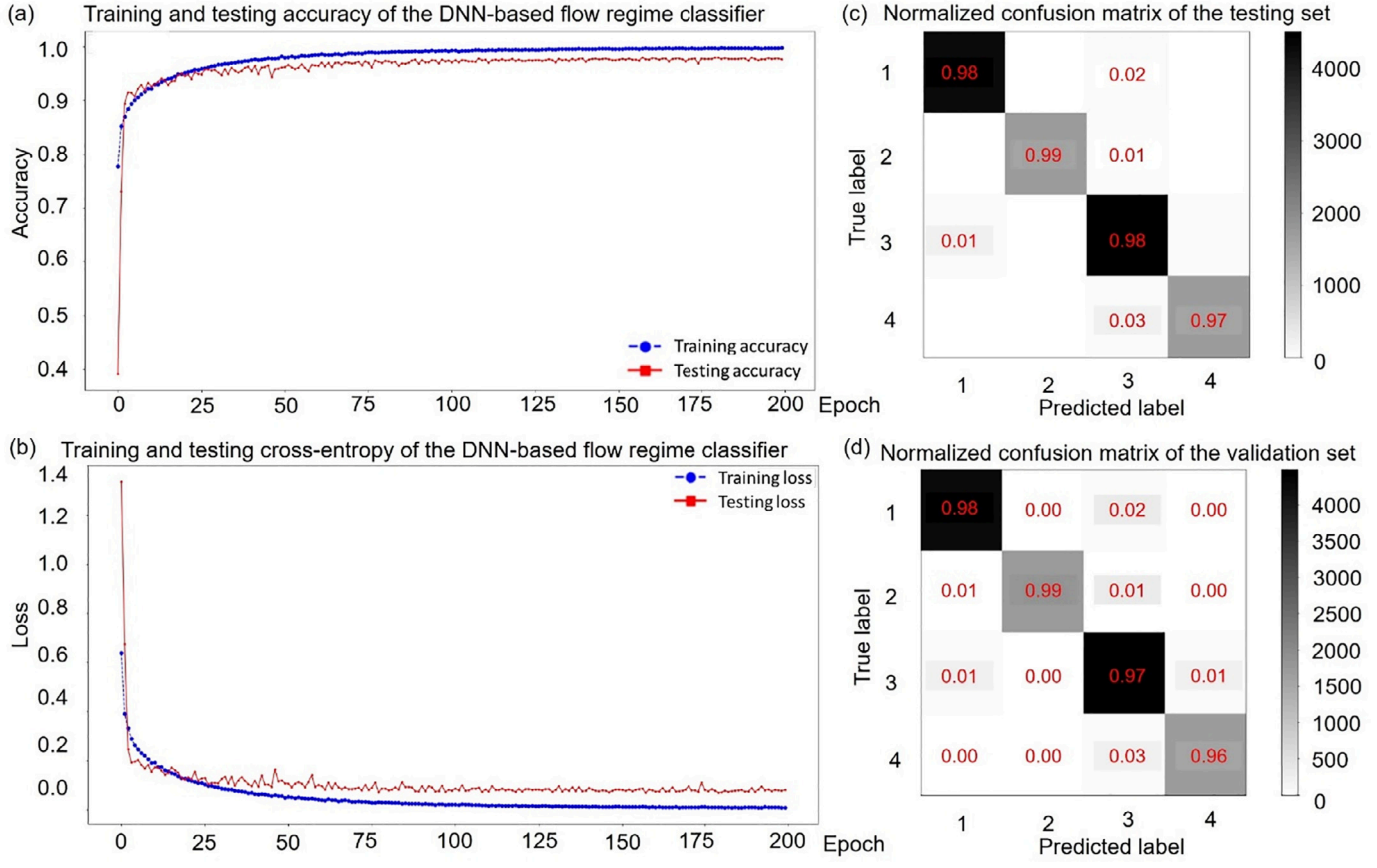

Fig. 22. The quantitative results of Experiment 12 in Tab. 2.

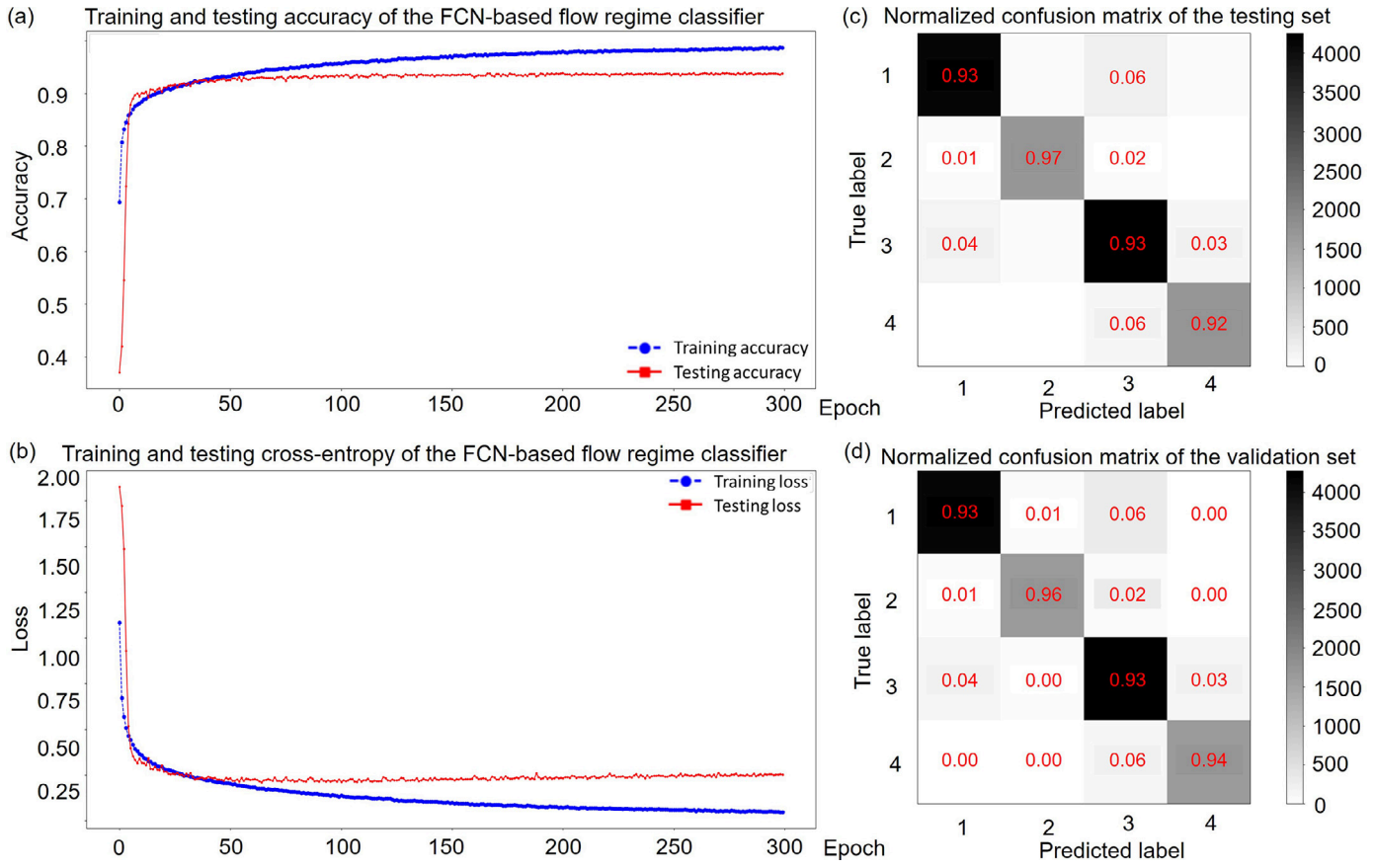

Fig. 23. The quantitative results of Experiment 13 in Tab. 2.

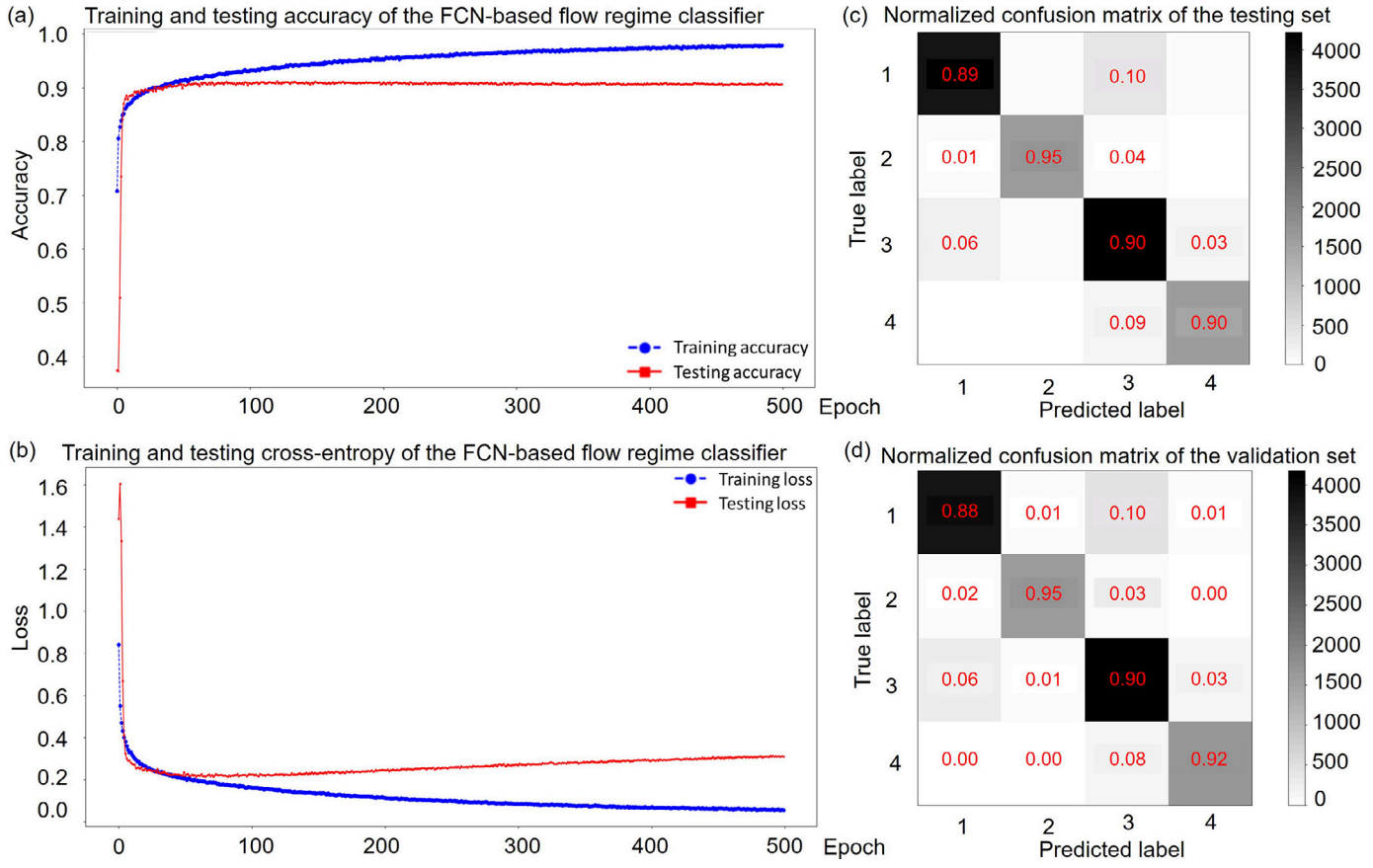

Fig. 24. The quantitative results of Experiment 14 in Tab. 2.

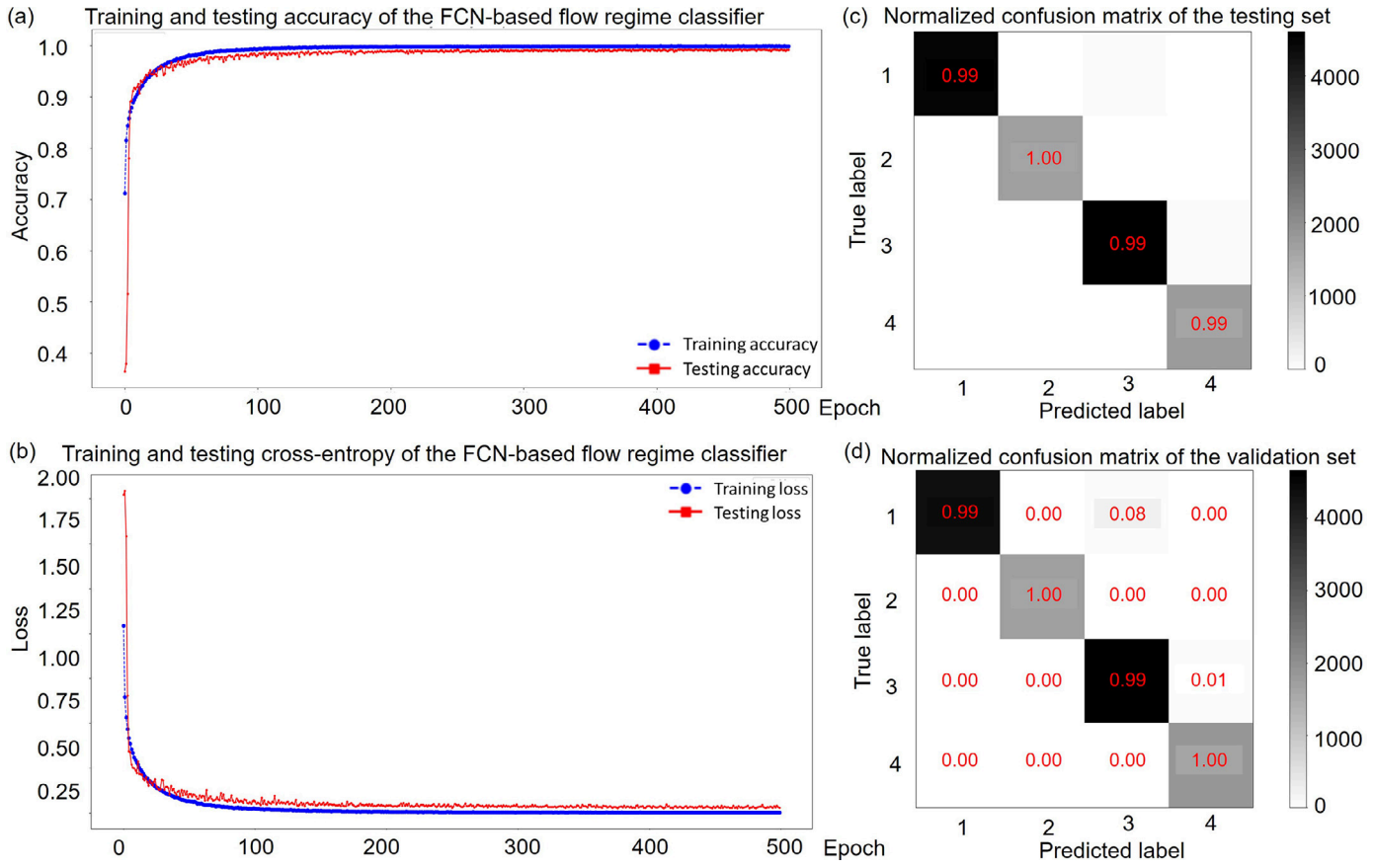

Fig. 25. The quantitative results of Experiment 15 in Tab. 2.

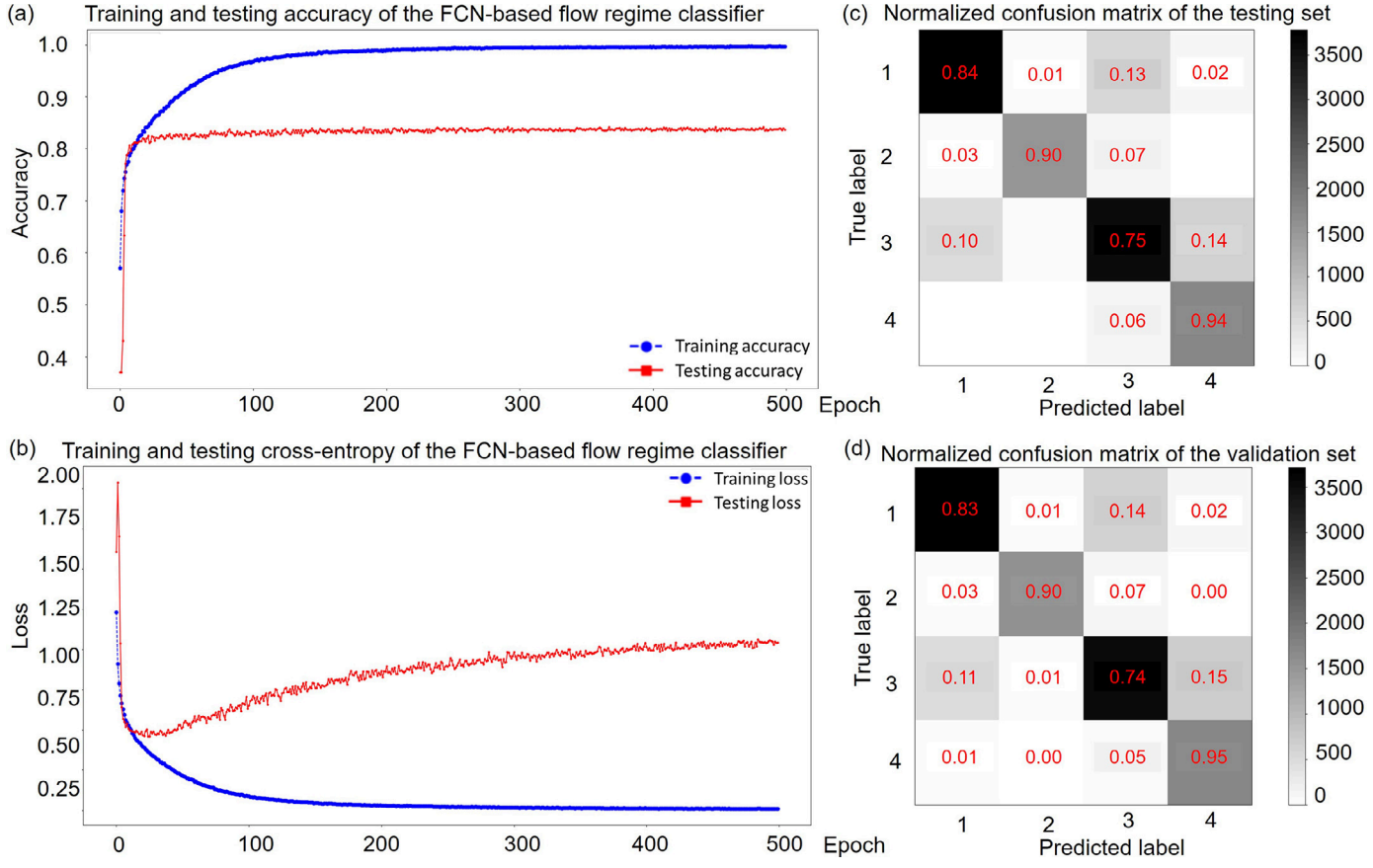

Fig. 26. The quantitative results of Experiment 16 in Tab. 2.

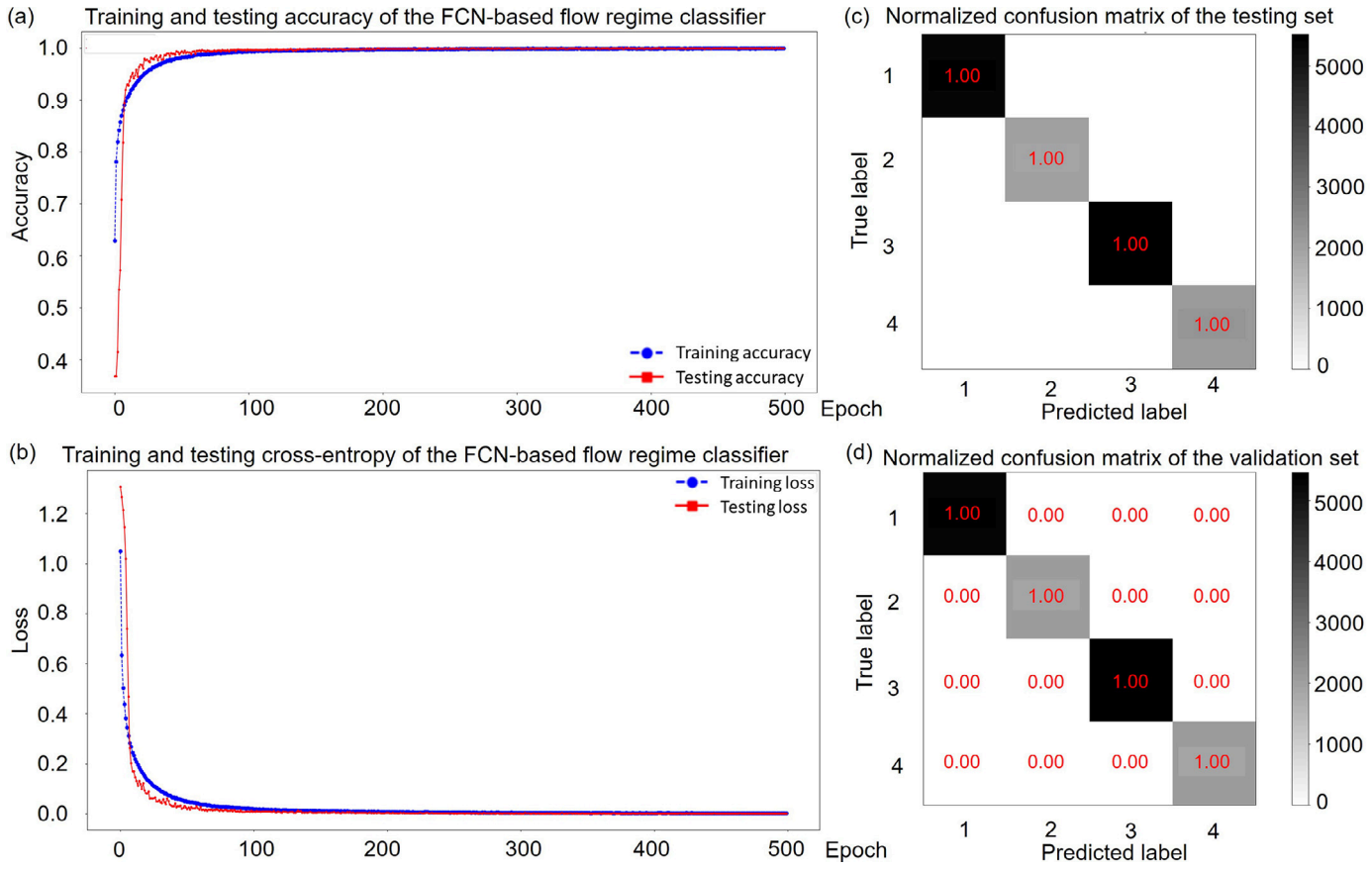

Fig. 27. The quantitative results of Experiment 17 in Tab. 2.

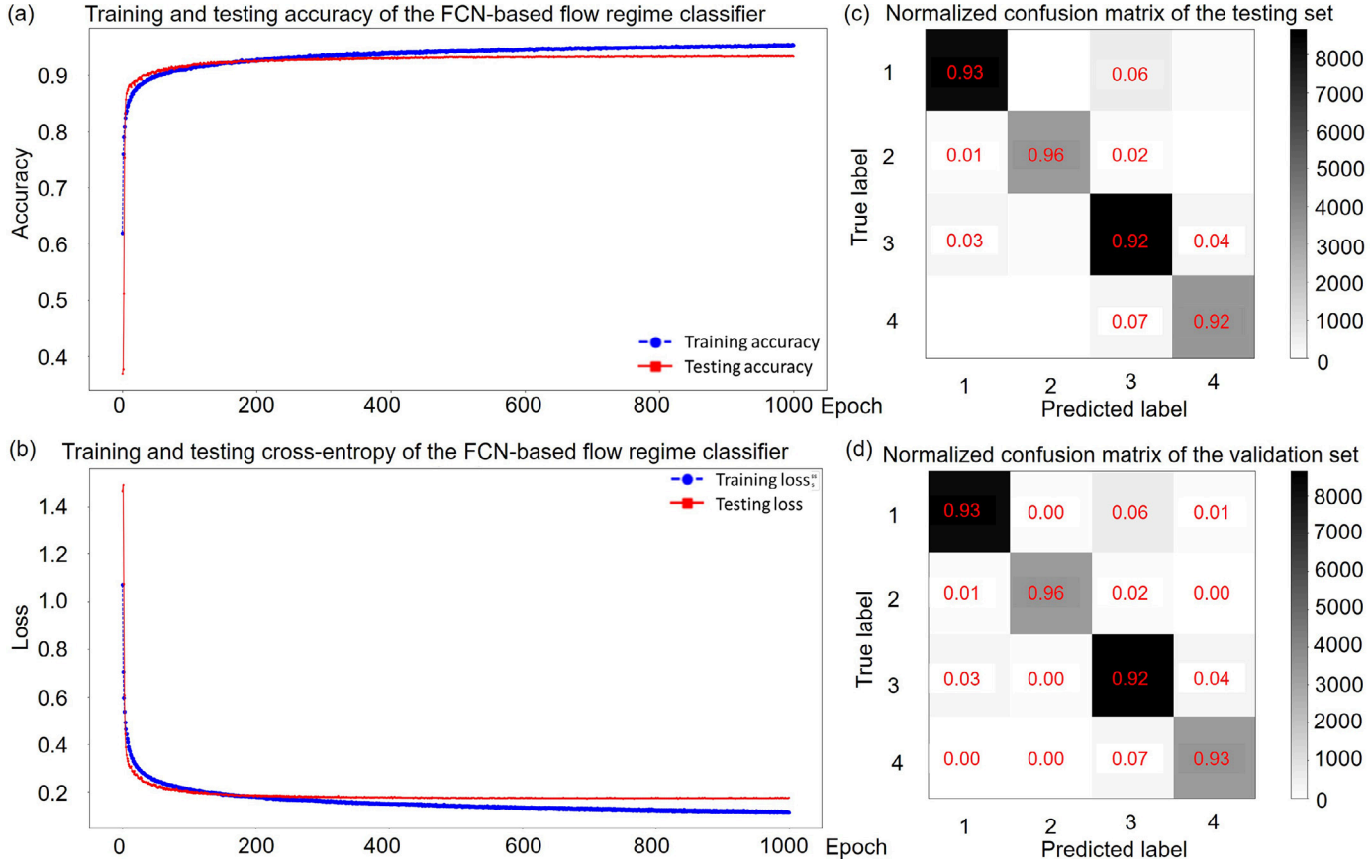

Fig. 28. The quantitative results of Experiment 18 in Tab. 2.

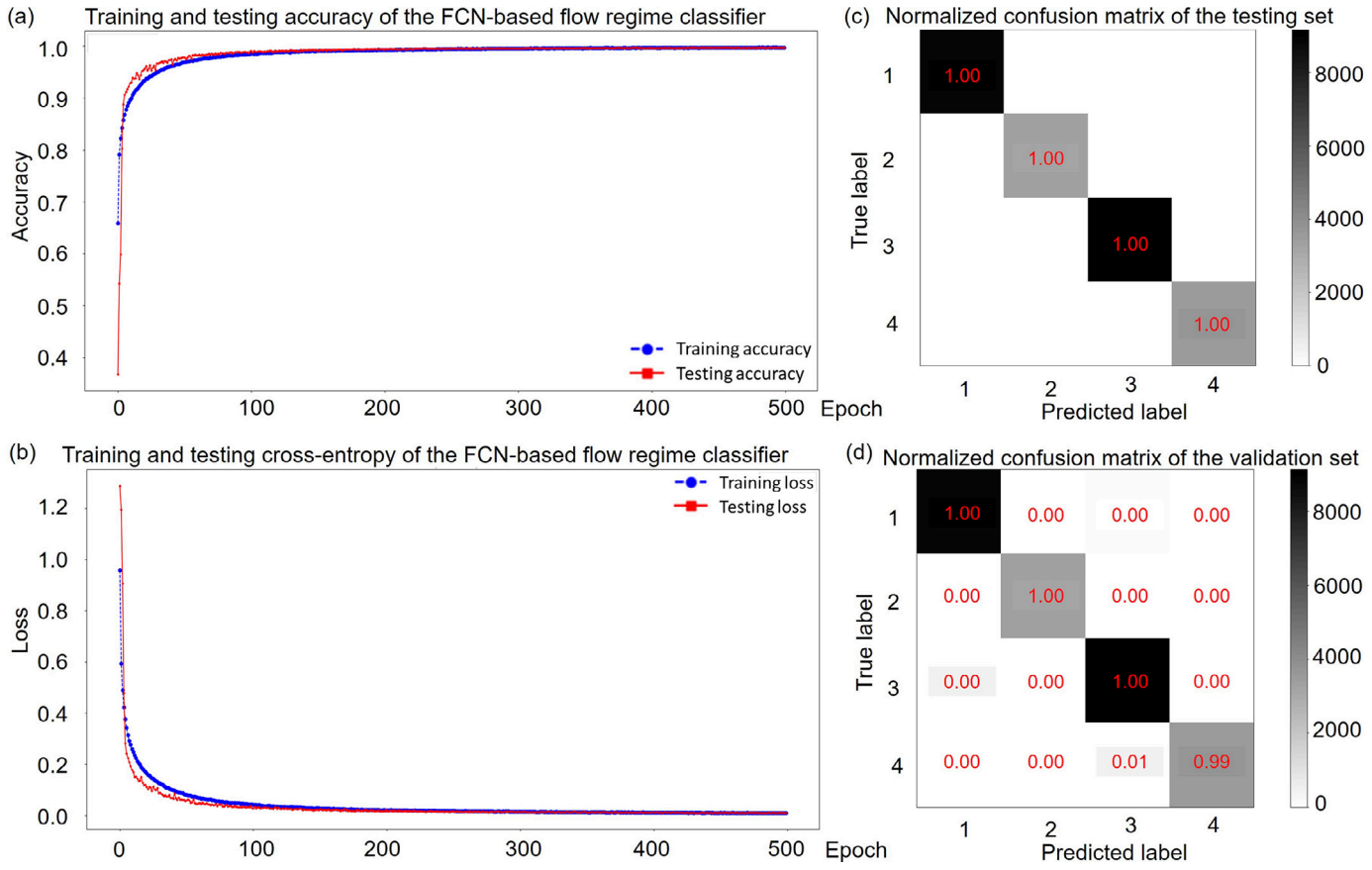

Fig. 29. The quantitative results of Experiment 19 in Tab. 2.

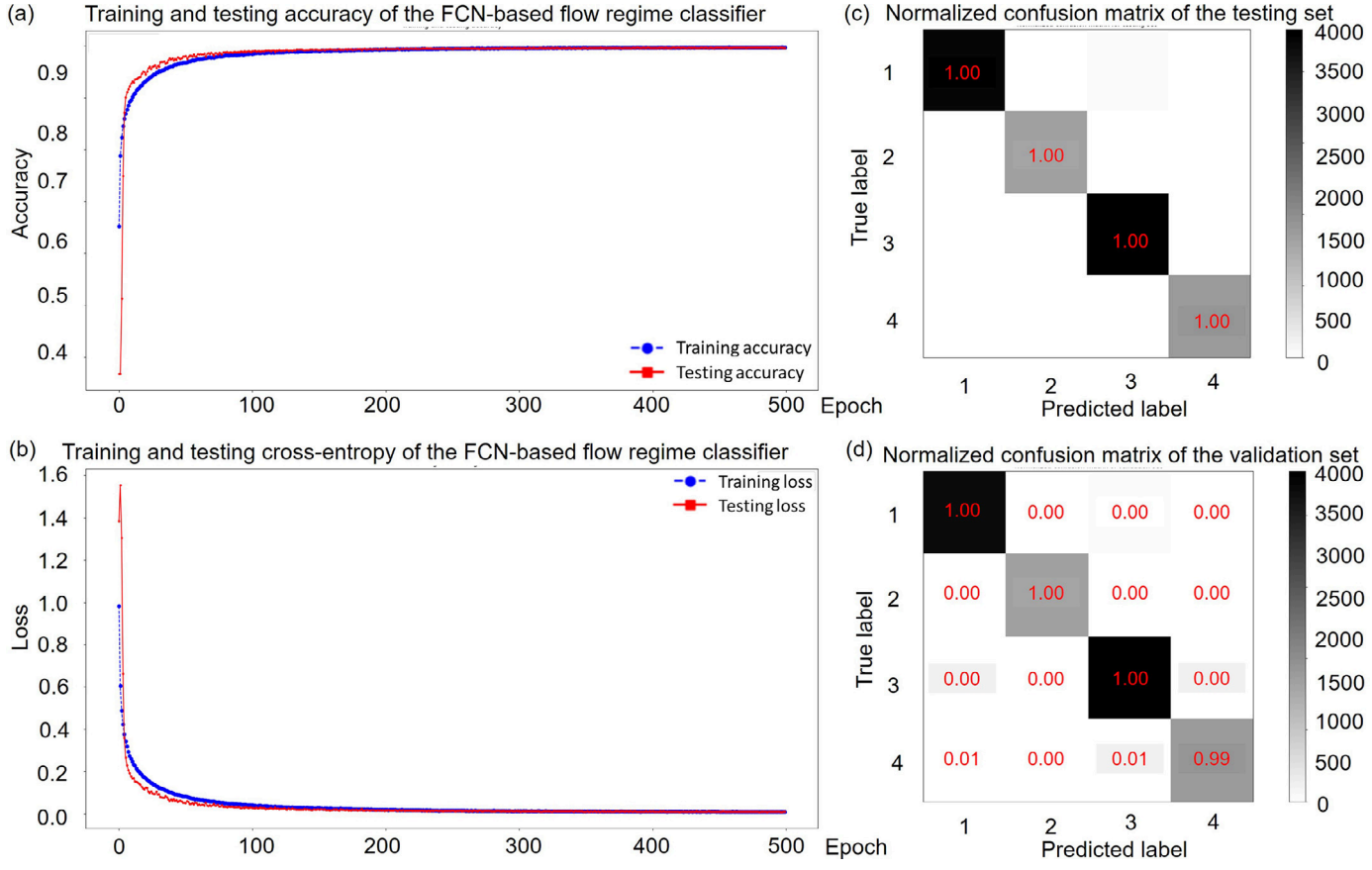

Fig. 30. The quantitative results of Experiment 20 in Tab. 2.

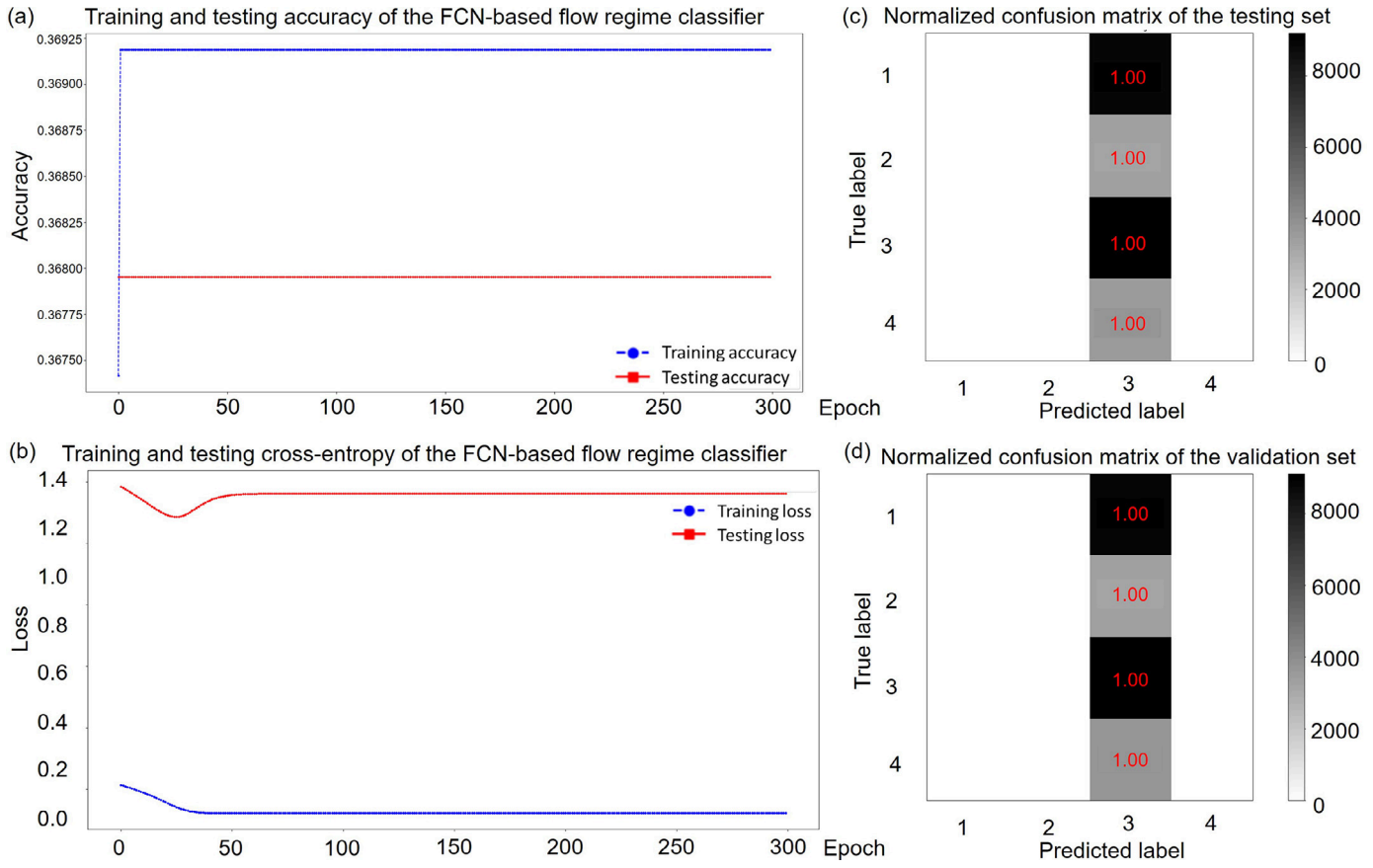

Fig. 31. The results of the VGG19 [20] network in Tab. 4.

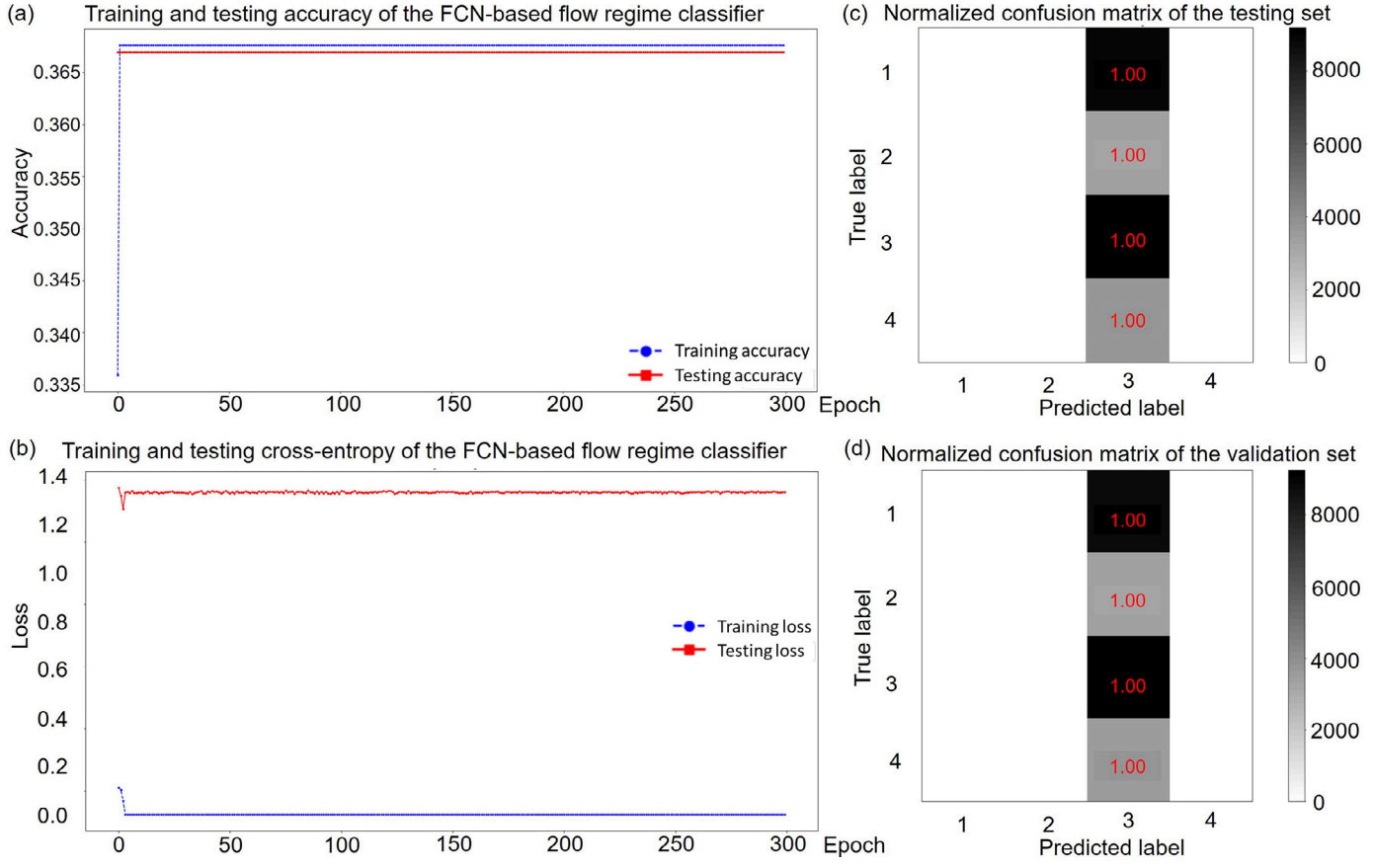

Fig. 32. The results of the pre+VGG19 [20] network in Tab. 4.

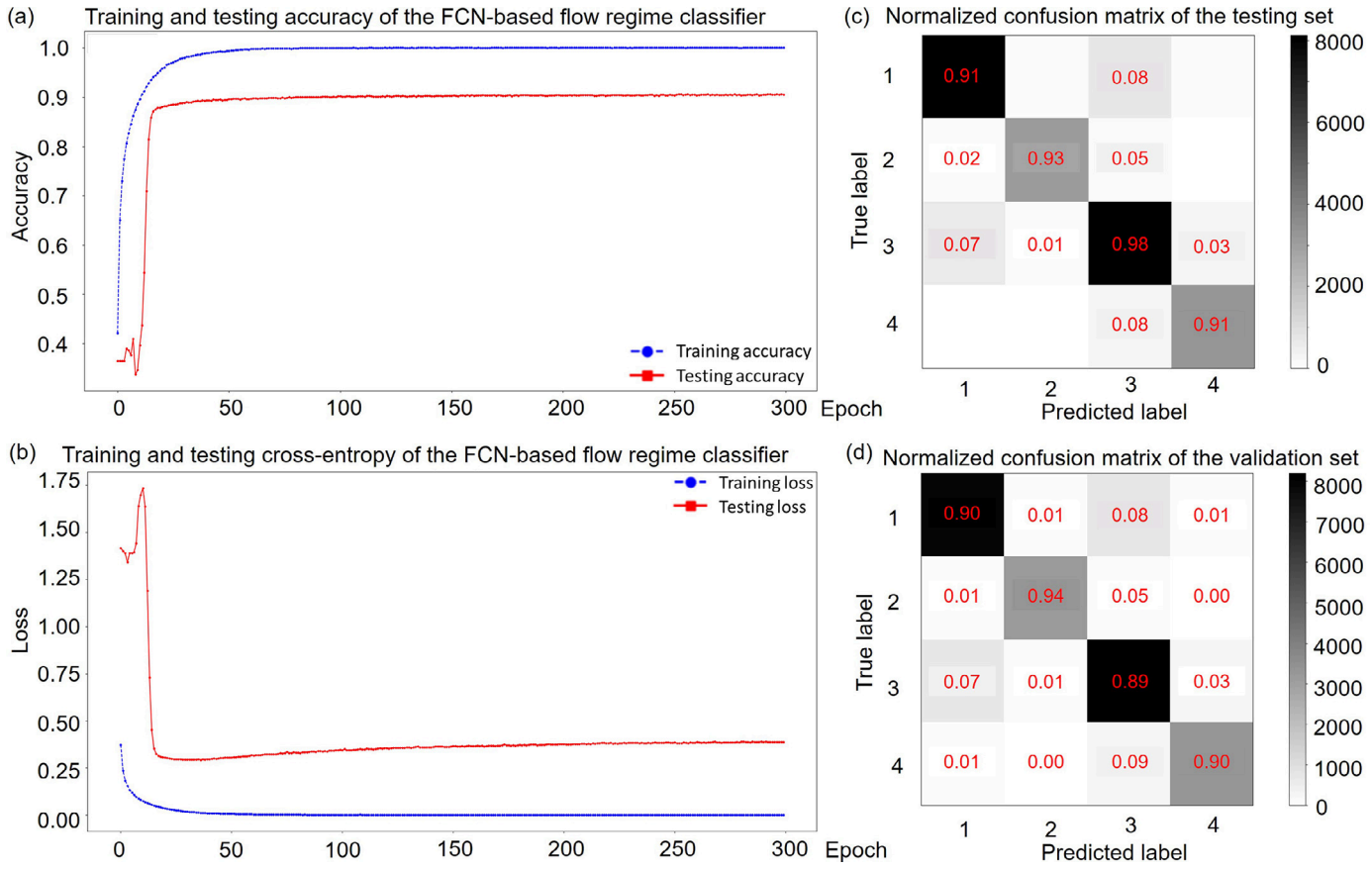

Fig. 33. The results of the ResNet50 [35] network in Tab. 4.

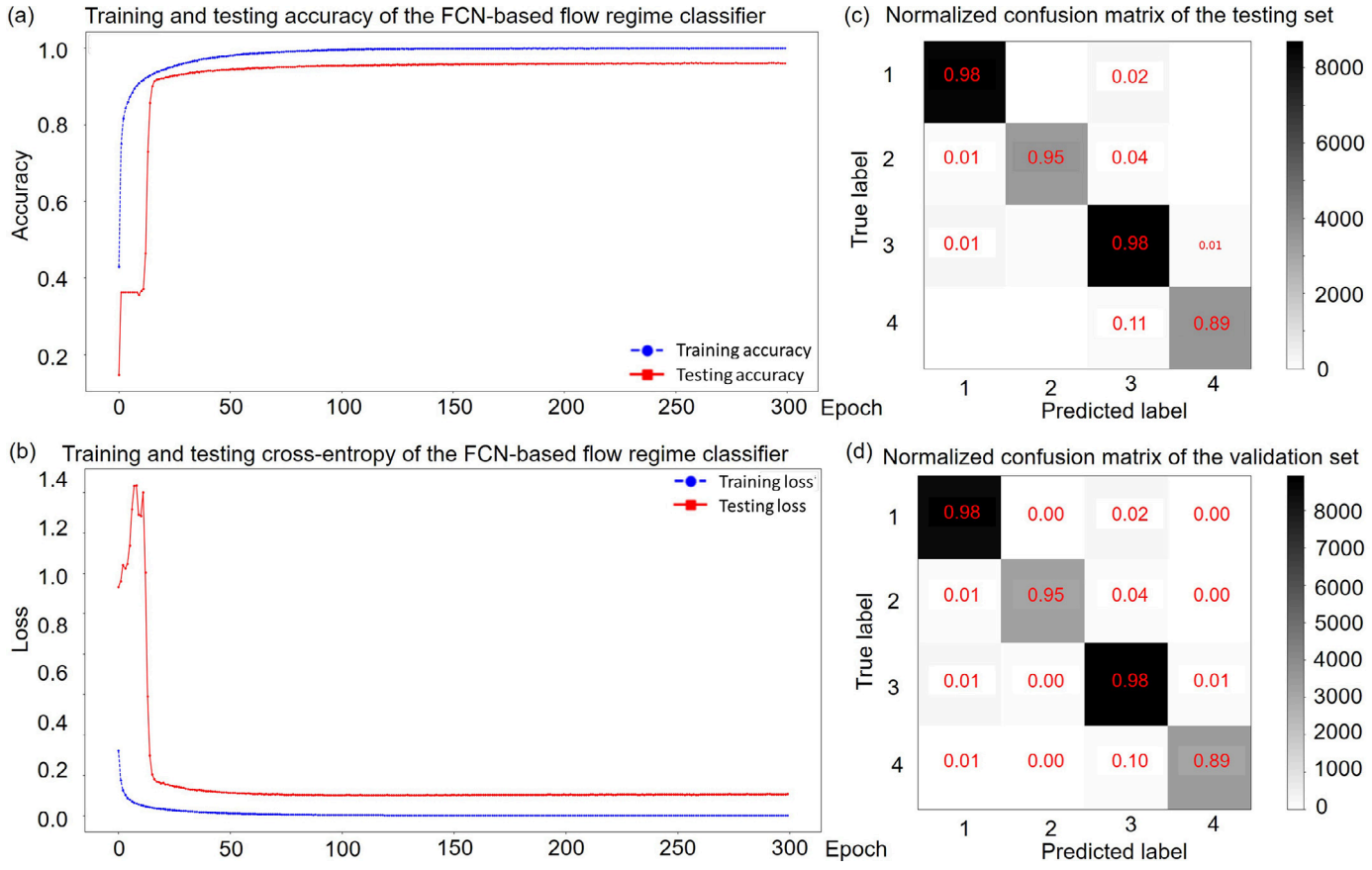

Fig. 34. The results of the DenseNet121 [36] network in Tab. 4.

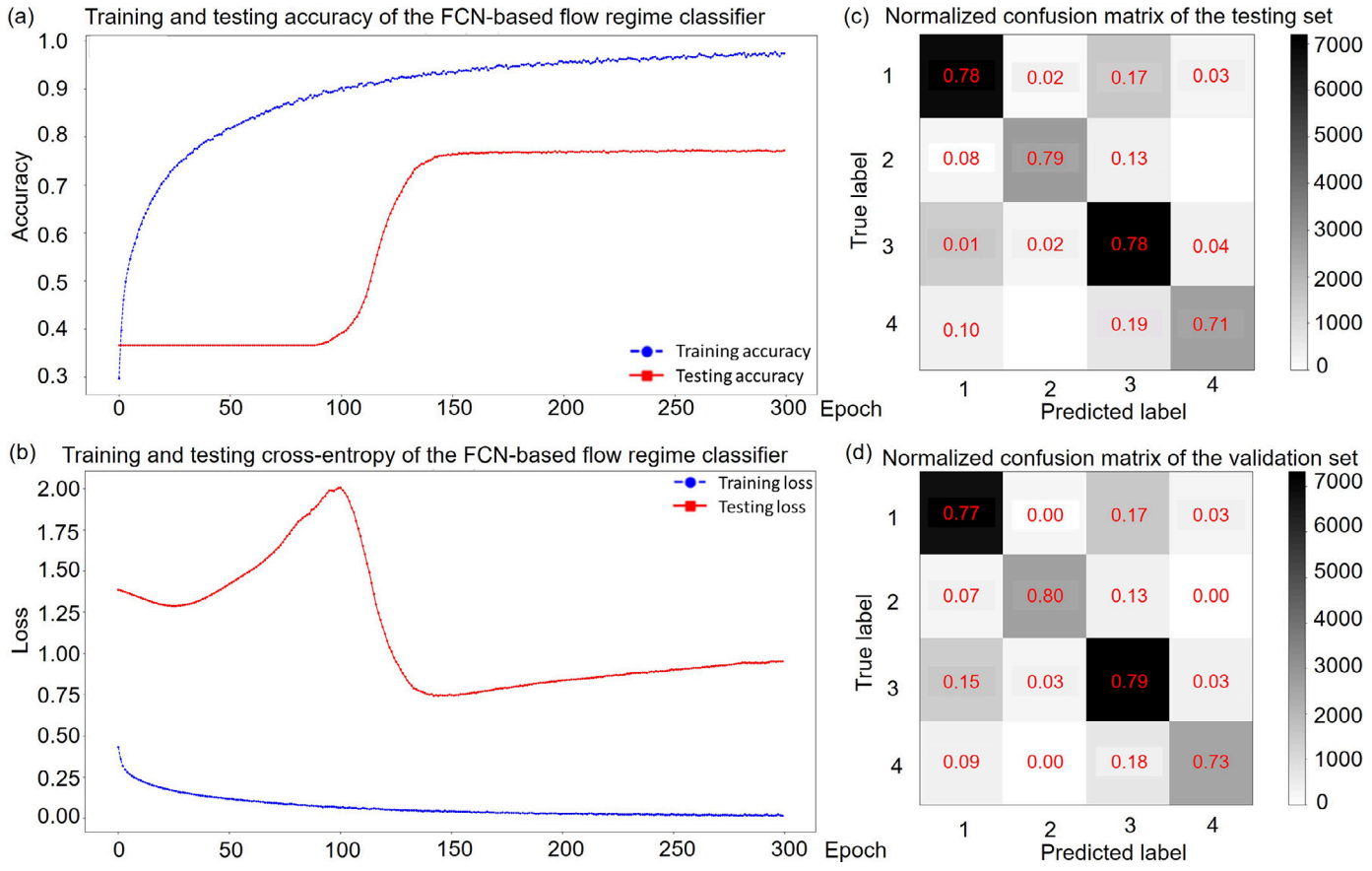

Fig. 35. The results of the MobileNet [37] network in Tab. 4.

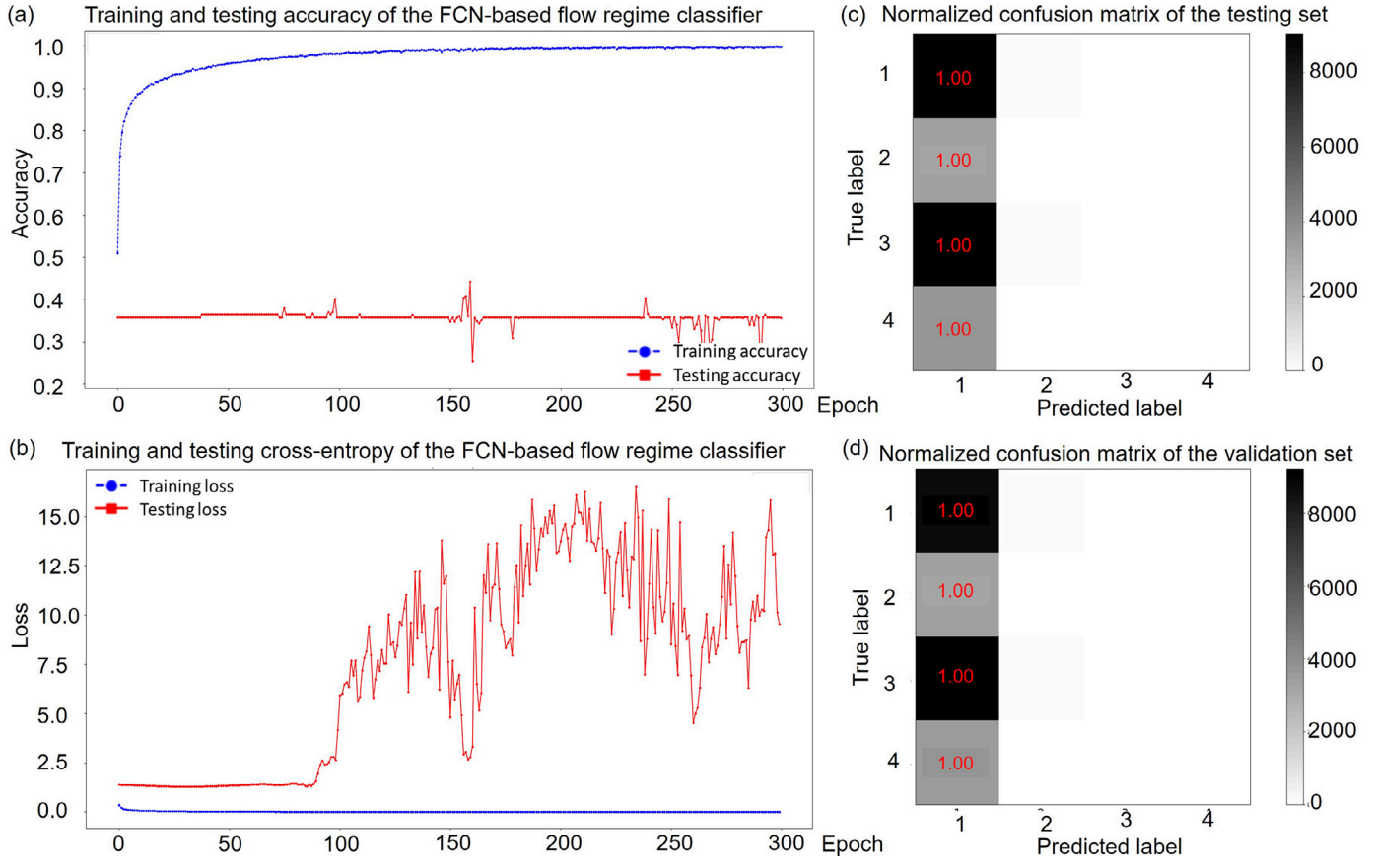

Fig. 36. The results of the pre+MobileNet [37] network in Tab. 4.

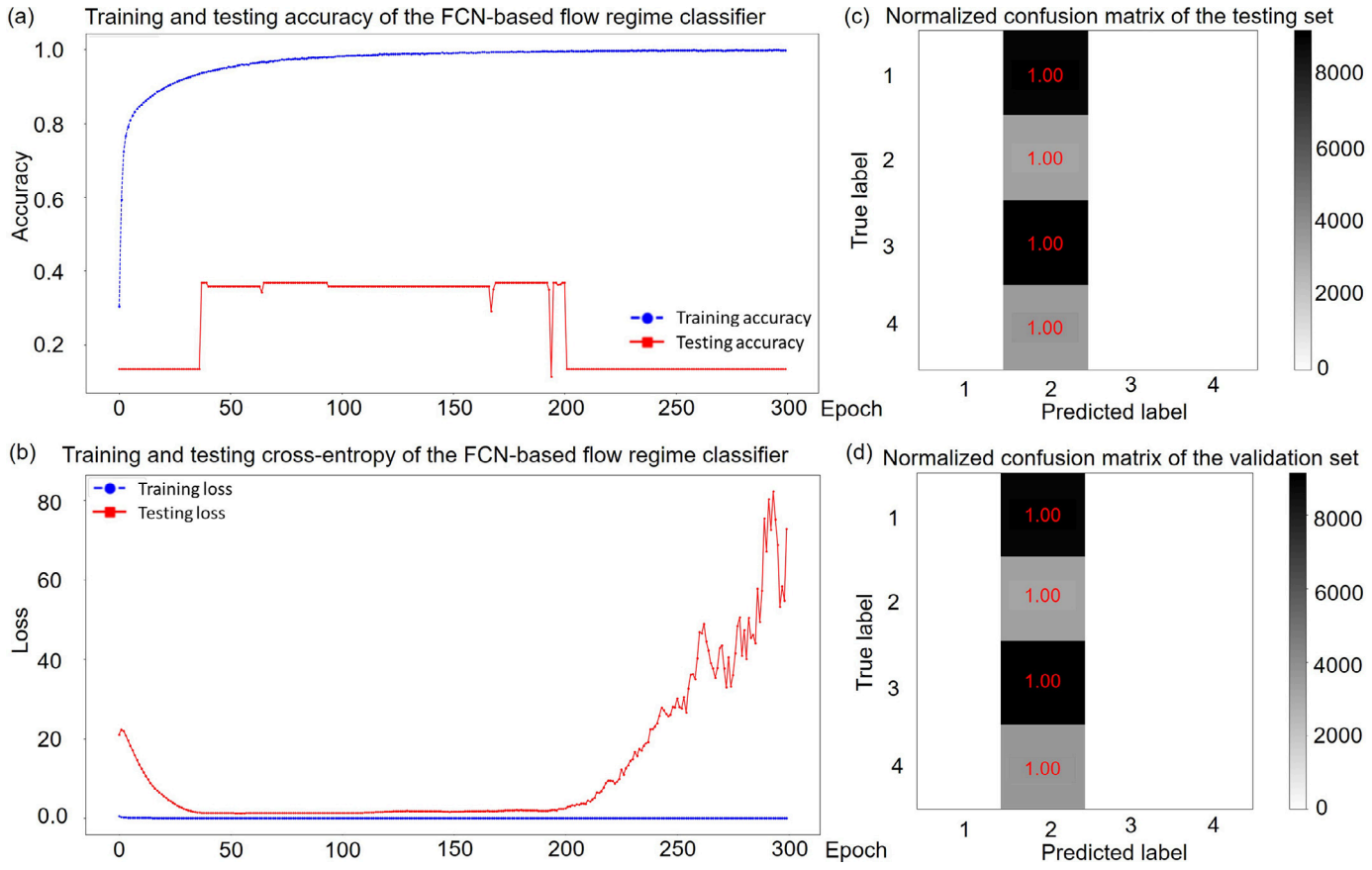

Fig. 37. The results of the NASNet [38] network in Tab. 4.

This paper further illustrates the specific data processing process in the FCN network in Fig. 4, which more intuitively depicts the analysis process of the PIF by the deep learning classifier. The four rows on the right side of Fig. 4 correspond to the processing details of the four flow-state PIFs in FCN. It is noteworthy that the distinguishing characteristics of different PIF flow regimes became increasingly explicit with the processing of FCN.

7. Conclusion

This research proposes the pseudo-image feature (PIF) and a flow regime identification benchmark for deep learning classifiers. The PIF encodes flow regime information more explicitly, which facilitates researchers' understanding of flow regime features from a more intuitive perspective. The three classifiers proposed in this paper performed better than all the tested popular classifiers, and they all surpassed the best existing algorithms. The FCN-based classifier achieved the best results, its training, testing, and verification accuracy reaching 99.95%, 99.95%, and 99.54%, respectively. This paper has graphically illustrated the detailed process of the proposed FCN classifier, which can facilitate an understanding of the exact process inside the classifier. Industries can utilize the proposed technology to obtain greater production efficiency, productivity, and financial gain.

Declaration of Competing Interest

The authors declared that they have no conflicts of interest to this work. We declare that we do not have any commercial or associative interest that represents a conflict of interest in connection with the work submitted.

Appendix

Algorithm: The pseudo-image feature (PIF) extraction algorithm
Input: $signal_{single}$, L_{WA}, S_{WA}, L_{WB-min}, L_{WB-max}, Δ_{WB}, S_{WB}, h, w
Output: PIF_{signal}

$L_{signal} \leftarrow$ the length of $signal_{single}$
$N_{WA} = N_{PIF} \leftarrow$ Eq. (4)
$c = N_{channel} \leftarrow$ Eq. (3)
function PIF_EXTRACTION($signal_{single}$, c)
$PIF_{signal} \leftarrow ZeroArray(N_{PIF}, h, w, c)$
$i = 0$
while $i < N_{WA}$ **do**
$WA \leftarrow signal_{single}[i^* S_{WA}, i^* S_{WA} + L_{WA}]$
$PIF_C \leftarrow ZeroArray(h, w, c)$
$k = 0$
while $k < c$ **do**
$feature_{C-sum} = 0$
$j = 0$
$L_{WB} = L_{WB-min} + i^* \Delta_{WB}$
$N_{WB} \leftarrow$ Eq. (2)
$feature_{C-sum} = 0$
$j = 0$
while $j < N_{WB}$ **do**
$freq_{WB} = 0$
$WB \leftarrow WA\ [k^* S_{WB}, k^* S_{WB} + L_{WB}]$
$freq_{WB} \leftarrow$ **fft**(WB, N_{fft})
$feature_{C-sum}$ += $freq_{WB}$
j += 1
end while
$feature_C = feature_{C-sum} / N_{WB}$
$PIF_{2D} \leftarrow$ **reshape**($feature_C$, [h, w, c])
$PIF_C[:,:,k] = PIF_{2D}$
k += 1
end while
$PIF_{signal}[i] = PIF_C$
i += 1
end while
return PIF_{signal}
end function

Reference

[1] M. Firouzi, S.H. Hashemabadi, Exact solution of two phase stratified flow through the pipes for non-Newtonian Herschel-Bulkley fluids, Int. Commun. Heat Mass Transf. 36 (7) (2009) 768–775.

[2] L. Cheng, G. Ribatski, J.R. Thome, Two-phase flow patterns and flow-pattern maps: fundamentals and applications, Appl. Mech. Rev. 61 (5) (2008) 050802.

[3] Q. Xu, W. Li, W. Liu, X. Zhang, C. Yang, L. Guo, Intelligent recognition of severe slugging in a long-distance pipeline-riser system, Exp. Therm. Fluid Sci. 113 (August 2019) (2020) 110022.

[4] D. Barnea, A unified model for predicting flow-pattern transitions for the whole range of pipe inclinations, Int. J. Multiph. Flow 13 (I) (1987) 1–12.

[5] Y. Tsuji, Y. Morikawa, Plug flow of coarse particles in ahorizontal pipe, J. Fluids Eng. 104 (2) (1982) 196–206.

[6] J. Weisman, S.. Kang, Flow pattern transition in vertical and upwardly inclined pipes, Int. J. Multiph. Flow 7 (3) (1981) 271–291.

[7] K.F. Hau, S. Banerjee, Measurement of mass flux in two-phase flow using combination of pitot tubes and gamma densitometers, AIChE J. 27 (2) (1981) 177–184.

[8] T. Dyakowski, Process tomography applied to multi-phase flow measurement, Meas. Sci. Technol. 7 (3) (1996) 343–353.

[9] Z.K. Gao, P.C. Fang, M.S. Ding, N. De Jin, Multivariate weighted complex network analysis for characterizing nonlinear dynamic behavior in two-phase flow, Exp. Therm. Fluid Sci. 60 (2015) 157–164.

[10] G. Zhongke, J. Ningde, Flow-pattern identification and nonlinear dynamics of gas-liquid two-phase flow in complex networks, Phys. Rev. E 79 (6) (2009) 066303.

[11] D.L. George, J.R. Torczynski, K.A. Shollenberger, T.J. O'Hern, S.L. Ceccio, Validation of electrical-impedance tomography for measurements of material distribution in two-phase flows, Int. J. Multiph. Flow 26 (4) (2000) 549–581.

[12] P.R. Tortora, S.L. Ceccio, T.J. O'Hern, S.M. Trujillo, J.R. Torczynski, Quantitative measurement of solids distribution in gas-solid riser flows using electrical impedance tomography and gamma densitometry tomography, Int. J. Multiph. Flow 32 (8) (2006) 972–995.

[13] S.A. Razzak, S. Barghi, J.X. Zhu, Application of electrical resistance tomography on liquid-solid two-phase flow characterization in an LSCFB riser, Chem. Eng. Sci. 64 (12) (2009) 2851–2858.

[14] C. Tan, F. Dong, M. Wu, Identification of gas/liquid two-phase flow regime through ERT-based measurement and feature extraction, Flow Meas. Instrum. 18 (5–6) (2007) 255–261.

[15] G.H. Roshani, E. Nazemi, S.A.H. Feghhi, S. Setayeshi, Flow regime identification and void fraction prediction in two-phase flows based on gamma ray attenuation, J. Int. Meas. Confed. 62 (1) (2015) 25–32.

[16] S. Kumar, D. Moslemian, M. Dudukovi ć, A γ-ray tomographic scanner for imaging voidage distribution in two-phase flow systems, Flow Meas. Instrum. 6 (1) (1995) 61–73.

[17] E. Dos Reis, L. Goldstein, A non-intrusive probe for bubble profile and velocity measurement in horizontal slug flows, Flow Meas. Instrum. 16 (4) (2005) 229–239.

[18] H. Canière, C. T'Joen, A. Willockx, M. De Paepe, Capacitance signal analysis of horizontal two-phase flow in a small diameter tube, Exp. Therm. Fluid Sci. 32 (3) (2008) 892–904.

[19] S. Huang, X. Zhang, D. Wang, Z. Lin, Equivalent water layer height (EWLH) measurement by a single-wire capacitance probe in gas-liquid flows, Int. J. Multiph. Flow 34 (9) (2008) 809–818.

[20] D.P. Chakrabarti, G. Das, P.K. Das, Identification of stratified liquid-liquid flow through horizontal pipes by a non-intrusive optical probe, Chem. Eng. Sci. 62 (7) (2007) 1861–1876.

[21] J. Oriol, J.P. Leclerc, C. Jallut, P. Tochon, P. Clement, Characterization of the two-phase flow regimes and liquid dispersion in horizontal and vertical tubes by using coloured tracer and non-intrusive optical detector, Chem. Eng. Sci. 63 (1) (2008) 24–34.

[22] S. Wada, H. Kikura, M. Aritomi, Pattern recognition and signal processing of ultrasonic echo signal on two-phase flow, Flow Meas. Instrum. 17 (4) (2006) 207–224.

[23] Y. Murai, Y. Tasaka, Y. Nambu, Y. Takeda, S.R. Gonzalez A., Ultrasonic detection of moving interfaces in gas-liquid two-phase flow, Flow Meas. Instrum. 21 (3) (2010) 356–366.

[24] S. Godfrey Nnabuife, B. Kuang, J.F. Whidborne, Z. Rana, Non-intrusive classification of gas-liquid flow regimes in an S-shaped pipeline riser using a Doppler ultrasonic sensor and deep neural networks, Chem. Eng. J. 403 (July 2020) (2020) 126401.

[25] E. Barrau, N. Rivière, C. Poupot, A. Cartellier, Single and double optical probes in air-water two-phase flows: Real time signal processing and sensor performance, Int. J. Multiph. Flow 25 (2) (1999) 229–256.

[26] S. Kim, X. Fu, X. Wang, M. Ishii, Development of the miniaturized four-sensor conductivity probe and the signal processing scheme, Int. J. Heat Mass Transf. 43 (22) (2000) 4101–4118.

[27] T.B. Trafalis, O. Oladunni, D.V. Papavassiliou, Two-phase flow regime identification with a multiclassification support vector machine (SVM) model, Ind. Eng. Chem. Res. 44 (12) (2005) 4414–4426.

[28] H. Ji, J. Long, Y. Fu, Z. Huang, B. Wang, H. Li, Flow pattern identification based on EMD and LS-SVM for gas - Liquid two-phase flow in a minichannel, IEEE Trans. Instrum. Meas. 60 (5) (2011) 1917–1924.

[29] J. Zhang, P.D. Roberts, On-line process fault diagnosis using neural network techniques, Trans. Inst. Meas. Control 14 (4) (1992) 179–188.

[30] S. Ghosh, D.K. Pratihar, B. Maiti, P.K. Das, Automatic classification of vertical counter-current two-phase flow by capturing hydrodynamic characteristics through objective descriptions, Int. J. Multiph. Flow 52 (2013) 102–120.

[31] S. Ghosh, D.K. Pratihar, B. Maiti, P.K. Das, Identification of flow regimes using conductivity probe signals and neural networks for counter-current gas – liquid two-phase flow, Chem. Eng. Sci. 84 (2012) 417–436.

[32] Y. Yan, L. Wang, T. Wang, X. Wang, Y. Hu, Q. Duan, Application of soft computing techniques to multiphase flow measurement: a review, Flow Meas. Instrum. 60 (2018) 30–43.

[33] D. Peng, B. Merriman, S. Osher, H. Zhao, M. Kang, A PDE-based fast local level set method, J. Comput. Phys. 155 (2) (1999) 410–438.

[34] K. Simonyan, A. Zisserman, Very deep convolutional networks for large-scale image recognition, Proc. IEEE Conf. Comput. Vis. Pattern Recognit. (2015) 1–14.

[35] K. He, X. Zhang, R. Shaoqing, J. Sun, Deep residual learning for image recognition, Proc. IEEE Conf. Comput. Vis. Pattern Recognit. (2015).

[36] G. Huang, K.Q. Weinberger, Densely connected convolutional networks, Proc. IEEE Conf. Comput. Vis. Pattern Recognit. (2018).

[37] M. Sandler, M. Zhu, A. Zhmoginov, C.V Mar, MobileNetV2: inverted residuals and linear bottlenecks, Proc. IEEE Conf. Comput. Vis. Pattern Recognit. (2019).

[38] B. Zoph, J. Shlens, Learning transferable architectures for scalable image recognition, Proc. IEEE Conf. Comput. Vis. Pattern Recognit. (2018).

[39] Z. Zhao, P. Zheng, Object detection with deep learning : a review, IEEE Trans. NEURAL NETWORKS Learn. Syst. (2019) 1–21.

[40] Y. Zhang, A. Nabilah, A. Ke, W. Xu, C. Kang, H. Bum, Two - phase flow regime identification based on the liquid - phase velocity information and machine learning, Exp. Fluids (2020) 1–16.

[41] J. Deng, W. Dong, R. Socher, L. Li, K. Li, and L. Fei-fei, "ImageNet : a large-scale hierarchical image database," pp. 248–255, 2009.

[42] X. Bangquan, W.X. Xiong, Real-time embedded traffic sign recognition using efficient convolutional neural network, IEEE Access 7 (2019) 53330–53346.

[43] N. Wang, D. Zhang, H. Chang, H. Li, Deep learning of subsurface flow via theory-guided neural network, J. Hydrol. 584 (January) (2020).

[44] Z. Lin, X. Liu, L. Lao, H. Liu, Prediction of two-phase fl ow patterns in upward inclined pipes via deep learning, Energy 210 (2020) 118541.

[45] H. Rahmanpanah, S. Mouloodi, C. Burvill, S. Gohari, H.M.S. Davies, Prediction of load-displacement curve in a complex structure using artificial neural networks: A study on a long bone, Int. J. Eng. Sci. 154 (2020) 103319.

[46] L. Fang, et al., Identification of two-phase flow regime using ultrasonic phased array, Flow Meas. Instrum. 72 (September 2019) (2020) 101726.

[47] B. Wu, M. Firouzi, T. Mitchell, T.E. Rufford, C. Leonardi, B. Towler, A critical review of flow maps for gas-liquid flows in vertical pipes and annuli, Chem. Eng. J. 326 (2017) 350–377.

[48] A. Peddu, S. Chakraborty, P. Kr. Das, Visualization and flow regime identification of downward air–water flow through a 12 mm diameter vertical tube using image analysis, Int. J. Multiph. Flow 100 (2018) 1–15.

[49] L. Liebenberg, J.P. Meyer, Objective classification of two-phase flow regimes, Heat Transf. Eng. (2008).

[50] E. Weinstein, Measurement of the differential Doppler shift, IEEE Trans. Acoust. 30 (1) (1982) 112–117.

[51] R.C. Chivers, C.R. Hill, A spectral approach to ultrasonic scattering from human tissue: methods, objectives and backscattering measurements, Phys. Med. Biol. 20 (3) (1975) 799–815.

[52] S.G. Nnabuife, J. Whidborne, L. Lao, Y. Cao, Venturi multiphase flow measurement based active slug control, in: ICAC 2019 - 2019 25th IEEE International Conference on Automation and Computing, 2019, pp. 1–6.

[53] S.G. Nnabuife, J. Whidborne, L. Lao, Two-phase gas-liquid flow regimes identification in an s-shape pipeline-riser using doppler ultrasonic sensor, Cranfield Online Research Data (CORD) Repository, Cranfield (2019).

[54] H. Tran-ngoc, S. Khatir, T. Le-xuan, G. De Roeck, T. Bui-tien, M. Abdel, A novel machine-learning based on the global search techniques using vectorized data for damage detection in structures, Int. J. Eng. Sci. 157 (2020).

[55] S.G. Nnabuife, K.E.S. Pilario, L. Lao, Y. Cao, M. Shafiee, Identification of gas-liquid flow regimes using a non-intrusive Doppler ultrasonic sensor and virtual flow regime maps, Flow Meas. Instrum. 68 (October 2018) (2019).

[56] A. Krizhevsky, G.E. Hinton, ImageNet Classification with Deep Convolutional Neural Networks, IEEE Conf. Comput. Vis. Pattern Recognit. (2009) 1–9.